**SANDIA REPORT**
SAND2013-10666
Unlimited Release
Printed December 2013

# A Micro to Macro Approach to Polymer Matrix Composites Damage Modeling: Final LDRD Report

Shawn English, Arthur Brown, Timothy Briggs

Prepared by
Sandia National Laboratories
Albuquerque, New Mexico 87185 and Livermore, California 94550

Sandia National Laboratories is a multi-program laboratory managed and operated by Sandia Corporation, a wholly owned subsidiary of Lockheed Martin Corporation, for the U.S. Department of Energy's National Nuclear Security Administration under contract DE-AC04-94AL85000.

Approved for public release; further dissemination unlimited.

Sandia National Laboratories

Issued by Sandia National Laboratories, operated for the United States Department of Energy by Sandia Corporation.

**NOTICE:** This report was prepared as an account of work sponsored by an agency of the United States Government. Neither the United States Government, nor any agency thereof, nor any of their employees, nor any of their contractors, subcontractors, or their employees, make any warranty, express or implied, or assume any legal liability or responsibility for the accuracy, completeness, or usefulness of any information, apparatus, product, or process disclosed, or represent that its use would not infringe privately owned rights. Reference herein to any specific commercial product, process, or service by trade name, trademark, manufacturer, or otherwise, does not necessarily constitute or imply its endorsement, recommendation, or favoring by the United States Government, any agency thereof, or any of their contractors or subcontractors. The views and opinions expressed herein do not necessarily state or reflect those of the United States Government, any agency thereof, or any of their contractors.

Printed in the United States of America. This report has been reproduced directly from the best available copy.

Available to DOE and DOE contractors from
U.S. Department of Energy
Office of Scientific and Technical Information
P.O. Box 62
Oak Ridge, TN 37831

Telephone: (865) 576-8401
Facsimile: (865) 576-5728
E-Mail: reports@adonis.osti.gov
Online ordering: http://www.osti.gov/bridge

Available to the public from
U.S. Department of Commerce
National Technical Information Service
5285 Port Royal Rd.
Springfield, VA 22161

Telephone: (800) 553-6847
Facsimile: (703) 605-6900
E-Mail: orders@ntis.fedworld.gov
Online order: http://www.ntis.gov/help/ordermethods.asp?loc=7-4-0#online

SAND2013-10666
Unlimited Release
Printed December 2013

# A Micro to Macro Approach to Polymer Matrix Composites Damage Modeling: Final LDRD Report

Shawn English
Arthur Brown
Timothy Briggs
Sandia National Laboratories
P.O. Box 969
Livermore, CA 94551-0969

**Abstract**

Capabilities are developed, verified and validated to generate constitutive responses using material and geometric measurements with representative volume elements (RVE). The geometrically accurate RVEs are used for determining elastic properties and damage initiation and propagation analysis. Finite element modeling of the meso-structure over the distribution of characterizing measurements is automated and various boundary conditions are applied. Plain and harness weave composites are investigated. Continuum yarn damage, softening behavior and an elastic-plastic matrix are combined with known materials and geometries in order to estimate the macroscopic response as characterized by a set of orthotropic material parameters. Damage mechanics and coupling effects are investigated and macroscopic material models are demonstrated and discussed. Prediction of the elastic, damage, and failure behavior of woven composites will aid in macroscopic constitutive characterization for modeling and optimizing advanced composite systems.

## CONTENTS


1. Introduction ..... 9

2. Materials ..... 11
   2.1. Continuum damage mechanics ..... 11
   2.2. General orthotropic damage and plasticity ..... 12
      2.2.1. Damage ..... 13
      2.2.2. Damage and Plastic Evolution ..... 15
   2.3. Transversely isotropic damage ..... 16
      2.3.1. Transversely Isotropic Elastic Damage ..... 16
      2.3.2. Thermodynamic Formulation ..... 18
   2.4. Micro-macro damage ..... 20
      2.4.1. Outline of constitutive equation ..... 20
      2.4.2. Constitutive Decomposition ..... 21
      2.4.3. Integration Scheme ..... 22
   2.5. Crack Band Theory ..... 24
   2.6. Polymer Matrix ..... 26

3. Experimental Results ..... 29
   3.1. Materials ..... 29
   3.2. Specimen Processing ..... 29
   3.3. Testing Procedure ..... 30
   3.4. Experimental Results ..... 30
   3.5. Experimental Requirements ..... 32

4. Mesh generation ..... 35
   4.1. Micromechanical ..... 35
   4.2. Mesomechanical ..... 38
      4.2.1. Yarn Orientations ..... 38
      4.2.2. Plain Weave Geometries ..... 40
      4.2.3. Satin Weave Geometries ..... 42
      4.2.4. Voxelization of 8HS RVE ..... 43

5. Boundary Conditions and Model Implementation ..... 45
   5.1. Boundary Conditions for RVEs ..... 45
   5.2. Verification ..... 46
      5.2.1. Boundary Conditions ..... 46
      5.2.2. Micro RVE Mesh Convergence ..... 49
      5.2.3. Meso RVE Mesh Convergence ..... 50
      5.2.4. Voxel Mesh Convergence ..... 52
      5.2.5. Elements ..... 53

6. Results and discussion ..... 55
   6.1. Elastic Properties ..... 55
      6.1.1. Plain-Weave Graphite-Epoxy ..... 55
      6.1.2. 8HS Glass-Epoxy ..... 56
      6.1.3. 8HS Carbon-Epoxy ..... 57
   6.2. Tensile loading of 8HS GFRP ..... 58

6.3. Shear loading of 8HS GFRP ..... 61
6.4. Damage/Plastic Properties from Shear ..... 62
6.5. Archives and Products ..... 65
6.5.1. Material Models ..... 65
6.5.2. Meshing ..... 65
6.5.3. Simulation and Post-Processing ..... 66

7. Conclusions and Future Work ..... 67

8. References ..... 69

Appendix A: Four volume edge generation ..... 71

Distribution ..... 75

## FIGURES

Figure 1. Tensile stress-strain relationships for various characteristic lengths. ..... 26
Figure 2. Mesh convergence results: peak load versus mesh size for an elliptically notched plate under tension. ..... 26
Figure 3. Estimated stress-strain relationship for UF3362-100 cured resin. ..... 27
Figure 4. GFRP 8-harness satin weave fiber surface with a unit cell illustrated. Warp face is shown with the warp direction vertically oriented. ..... 29
Figure 5. Tensile testing specimen geometry ..... 30
Figure 6. Front edge micrograph detailing warp fiber tow ends ..... 31
Figure 7. Unit cell from the top surface of an as-cured laminate ..... 31
Figure 8. Tensile stress-strain curves for the warp and weft directions of a GFRP ..... 32
Figure 9. Tensile warp stress-strain curves two GFRP with different manufacturing techniques (data from Wei-Yang Lu) ..... 33
Figure 10. Fiber volume fraction versus resin mass fraction for GFRP and CFRP ..... 33
Figure 11. RVE von Mises stress distribution under uniaxial transverse tension, a) peak load and b) post fracture ..... 35
Figure 12. Homogenized tensile response for multiple samplings with a coarse mesh at $v_f$ = 67% ..... 36
Figure 13. RVE size convergence of transverse modulus for random fiber composites ..... 37
Figure 14. Illustration of the stages of crack development in the constitutive model ..... 38
Figure 15. Illustration of the orientation optimization ..... 39
Figure 16. Output orientations for a yarn segment at symmetry plane written to each integration point ..... 40
Figure 17. Yarns of an 8-harness satin weave ..... 43
Figure 18. Voxelized mesh of an 8-harness satin weave shown without matrix ..... 44
Figure 19. In-plane shear loading of a plain weave RVE with cohesive zone interface failure and material shear stress contours (matrix and cohesive elements not shown) ..... 46
Figure 20. Homogenized tensile response for single coarse sample with different mesh sizes .. 49
Figure 21. Mesh convergence of uniaxial transverse peak load for random fiber composites .... 50
Figure 22. Transverse modulus verse mesh size ratio for a random glass fiber model ..... 50
Figure 23. Mesh convergence of the volume average shear stress at $\gamma_{12}$ = 2.16 % for a plain weave geometry ..... 51

Figure 24. 8HS GFRP elastic properties voxel mesh convergence plot ..... 53
Figure 25. Distribution of the axial modulus ..... 56
Figure 26. Transverse (fill) yarn cracks shown as failed elements in red ..... 59
Figure 27. Crack cloud experimental example for GFRP under uniaxial tension ..... 59
Figure 28. Stress versus strain for axial (warp) tension in GFRP 8HS ..... 59
Figure 29. Approximate uniformly distributed transverse strengths for unidirectional GFRP ... 61
Figure 30. Stress versus strain for the in-plane shear of GFRP 8HS ..... 62
Figure 31. Transverse damage distribution of a plain weave RVE under pure in-plane shear (shown without matrix) ..... 62
Figure 32. Cyclic shear response of a plain weave RVE ..... 63
Figure 33. Damage accumulation under shear ..... 64
Figure 34. Plastic strain accumulation under shear ..... 64

## TABLES

Table 1. In-plane shear moduli 8HS GFRP ..... 51
Table 2. Max out-of-plane displacement of a GFRP 8HS for $\Delta T = 50$ C ..... 52
Table 3. Max stress of a unloaded GFRP 8HS for $\Delta T = 50$ C ..... 52
Table 4. Carbon-epoxy plain weave elastic properties ..... 55
Table 5. E-glass 8HS elastic properties ..... 57
Table 6. Unidirectional CFRP (yarn) properties ..... 57
Table 7. 8HS CFRP elastic properties ..... 58
Table 8. Unidirectional GFRP (yarn) elastic properties ..... 58

# NOMENCLATURE

| | |
|---|---|
| RVE | Representative Volume Element |
| PCM | Polymer Matrix Composite |
| CDM | Continuum Damage Mechanics |
| HS | Harness Satin |
| GFRP | Glass Fiber Reinforced |
| CFRP | Carbon Fiber Reinforced |
| CTE | Coefficient of Thermal Expansion |

# 1. INTRODUCTION

While proper material characterization requires a great deal of experiments, often preliminary scoping and design requires only broad statistical bounds of the material parameters. Thus, the presented micro/mesomechanical material characterization procedures are not intended to replace experiments, but rather supplement the often expensive and difficult to obtain data required for even the most basic material scoping and initial design processes.

A distribution of constitutive responses is obtained for polymer matrix composites (PCM) using material and geometric measurements with representative volume elements (RVE). The geometrically accurate RVEs are used for detailed stress concentration and damage initiation and propagation analysis. Finite element modeling of the meso-structure over the distribution of characterizing measurements is automated and various boundary conditions are applied. Plain and eight-harness satin (8HS) weave glass fiber reinforced (GFRP) and carbon fiber reinforced (CFRP) polymer composites are implemented. Continuum yarn damage, inter-yarn debonding and an elastic-plastic matrix are combined with known materials and geometries in order to estimate the macroscopic response as characterized by a set of orthotropic material parameters. Damage mechanics and coupling effects are investigated and a macroscopic material model is demonstrated and discussed. Prediction of the elastic, damage, and failure behavior of woven composites will aid in macroscopic constitutive characterization for modeling and optimizing advanced composite systems.

Macroscopic constitutive relations for composite damage evolution analysis are abundant in the literature [1-6]. Fully characterizing even the most common damage evolution and failure models requires difficult to implement experiments. In addition to elastic characterization, an approach is presented to obtain estimates of the damage/plastic initiation/evolution parameters.

The constituent (fiber, matrix) properties are often given in literature, manufacturing specifications or can be determined by a few simple tests. Validating/calibrating experiments are then used in conjunction with geometrically accurate micro/mesomechanical simulations. Additional loading conditions are then applied to the numerical model in order to further characterize the macroscopic response of the material.

This document is laid out as follows: First, the constitutive models and material modeling techniques developed for or in conjunction with this project are described in detail. Second, the experimental results obtained through Sandia resources and those acquired from literature are listed. In addition, the minimum and ideal characterization requirements for micro to macro modeling are discussed. Third, the geometry and model development and implementation are described. Lastly, verification of mesh and modeling techniques as well as validation using simple experiments are presented.

# 2. MATERIALS

In general, the constituents of the PCM are simply the fibers and matrix. Therefore, given micro-geometric details, an RVE of a PCM can be modeled with only two material responses. This over simplification is not valid, however, when dealing with non-linear responses because material interfaces and multiple scales (woven composites) are involved.

Three specific material models will be discussed in this report. The first is a general orthotropic elastic damage model that is fully documented in [7]. The basic theoretical background and extension to coupled plasticity will be discussed. The second is a micro to macro continuum damage model described in [8]. The implementation and theoretical background are given in detail to demonstrate techniques and potential uses for this research. The third is a transversely isotropic continuum damage model based on [4, 5, 9]. This model is specifically implemented to simulate yarn damage in fabric reinforced geometries. For simple load cases, damage only occurs in the orthotropic lamina planes. However, a general transversely isotropic model can provide higher accuracy under more complex loadings where the crack plane is unknown.

## 2.1. Continuum damage mechanics

The following outlines the basic thermodynamic formulation of a continuum damage mechanics (CDM) material model. This write-up was also presented in more detail in [7] and in the references [1-3].

The material response is modeled by relating the Green-Lagrange strain ($E$) to the second Piola-Kirchhoff stress ($S$). This is called a Saint-Venant-Kirchhoff (Kirchhoff) material and is valid for small strains and large rotations [10].

$$S_{ij} = \boldsymbol{C}_{ijkl} E_{kl}$$

The local Clausius-Duhem inequality ensuring a positive internal entropy production is written in terms of the Helmholtz free energy ($\psi$)

$$-\rho\dot{\psi} - \rho\dot{\mathrm{T}}\eta + \mathrm{S}:\dot{\mathrm{E}} - \mathrm{Tq}\cdot\nabla\mathrm{T}^{-1} \geq 0$$

where $\rho$ is density, $\eta$ is entropy, and q is the heat flux. The Helmholtz free energy is a function of elastic strain, temperature, damage and internal state variables ($\psi(E, T, D, \delta)$). Applying the chain rule, the above equation becomes

$$\left(-\rho\frac{\partial\psi}{\partial\mathrm{E}} + \mathrm{S}\right):\dot{\mathrm{E}} - \rho\left(\frac{\partial\psi}{\partial\mathrm{T}} + \eta\right)\dot{\mathrm{T}} - \rho\frac{\partial\psi}{\partial\mathrm{D}}\dot{\mathrm{D}} - \rho\frac{\partial\psi}{\partial\delta}\dot{\delta} - \mathrm{Tq}\cdot\nabla\mathrm{T}^{-1} \geq 0$$

where the tensor $D$ and the scalar $\delta$ are internal state variables associated with damage. The Helmholtz free energy density $\psi$ is assumed to be the sum of the strain energy density $\varphi$ and a dissipation term $\pi$

$$\psi\left(E_{ij}, T, D_{ij}, \delta\right) = \varphi\left(E_{ij}, T, D_{ij}\right) + \pi(\delta)$$

The following thermodynamic forces are defined

$$S_{ij} = \rho \frac{\partial \psi}{\partial E_{ij}} = \boldsymbol{C}_{ijkl} E_{kl}$$

$$\eta = -\frac{\partial \psi}{\partial T}$$

$$Y_{ij} = \frac{\partial \psi}{\partial D_{ij}} = -\frac{1}{2} E_{kl} \frac{\partial C_{klpq}}{\partial D_{ij}} E_{pq}$$

where $Y_{ij}$ is the thermodynamic force conjugate to damage, and damage is defined as crack area over total area.

## 2.2. General orthotropic damage and plasticity

A useful addition to the elastic CDM approach is the evolution of plastic strains. While composites under normal loading typically exhibit quasi-brittle fracture, shear deformation can produce the appearance of plastic strains. Similar to the above formulation, the Helmholtz free energy density $\psi$ is assumed to be the sum of the strain energy $\varphi$ density and a dissipation term $\pi$

$$\psi\left(\varepsilon_{ij}, \varepsilon_{ij}^{p}, p, D_{ij}, \delta\right) = \varphi\left(\varepsilon_{ij}, \varepsilon_{ij}^{p}, D_{ij}\right) + \pi(p, \delta)$$

where $\varepsilon_p$ and $D_{ij}$ are plastic strain and damage tensors respectively and $p$ and $\delta$ are the plastic and damage evolution terms. In this and the following cases, the strain will be assumed small and generalized as $\varepsilon_{ij} = E_{ij}$. The dissipation term is separable into plastic strain energy and damage energy dissipation portions.

$$\pi(p, \delta) = \pi_d(\delta) + \pi_p(p)$$

A Prony series is postulated to represent these terms

$$\pi_d(\delta) = \sum_{i=1}^{n} \alpha_i^d \left[-\beta_i^d exp\left(\frac{\delta}{\beta_i^d}\right) + \delta\right]$$
$$\pi_p(p) = \sum_{i=1}^{n} \alpha_i^p \left[-\beta_i^p exp\left(\frac{p}{\beta_i^p}\right) + p\right]$$

where $\alpha_i$ and $\beta_i$ are material parameters determined by curve fits of experimental data.

The following stresses and thermodynamic forces are defined

$$\sigma_{ij} = \rho \frac{\partial \psi}{\partial \varepsilon_{ij}^{e}} = C_{ijkl}\varepsilon_{kl}^{e}$$

$$Y_{ij} = \rho \frac{\partial \psi}{\partial D_{ij}} = -\frac{1}{2}\varepsilon_{kl}^{e}\frac{\partial C_{klpq}}{\partial D_{ij}}\varepsilon_{pq}^{e}$$

where

$$\varepsilon_{ij}^{e} = \varepsilon_{ij} - \varepsilon_{ij}^{p}$$

The hardening functions are given by

$$\gamma(\delta) = -\frac{\partial \psi}{\partial \delta} = \sum_{i=1}^{n} \alpha_i^d \left[ exp\left(\frac{\delta}{\beta_i^d}\right) - 1 \right]$$

$$R(p) = -\frac{\partial \psi}{\partial p} = \sum_{i=1}^{n} \alpha_i^p \left[ exp\left(\frac{p}{\beta_i^p}\right) - 1 \right]$$

### *2.2.1. Damage*

For many composite materials, damage occurs only on principal material planes. Therefore, the damage parameters can be limited to those effecting the normal and transverse principal material directions. The second order damage tensor $D_{ij}$ and the associated integrity tensor $\Omega_{ij}$ and damage effects tensor $M_{ijkl}$ are defined as:

$$D_{ij} = \begin{bmatrix} d_{11} & 0 & 0 \\ 0 & d_{22} & 0 \\ 0 & 0 & d_{33} \end{bmatrix}$$

$$\Omega_{ij} = \begin{bmatrix} \sqrt{1-d_{11}} & 0 & 0 \\ 0 & \sqrt{1-d_{22}} & 0 \\ 0 & 0 & \sqrt{1-d_{33}} \end{bmatrix}$$

$$M_{ijkl} = \frac{1}{2}\left(\Omega_{ik}\Omega_{jl} + \Omega_{il}\Omega_{jk}\right)$$

For unidirectional composites, coupling of shear and normal damage is a result of micro-cracks, fiber breaks and fiber-matrix deboning as in the above formulation. However, some materials may not experience a linear coupling between normal and shear damage. For example, plane weave composites under shear experience stiffness reduction due to matrix cracking and fiber-matrix deboning with little to no fiber breakage resulting in only a minor reduction of stiffness in the fiber directions. For fully normal and shear uncoupled analysis $D_{ij}$, $\Omega_{ij}$ and $M_{ijkl}$ can be is defined as

$$D_{ij} = \begin{bmatrix} d_{11} & d_{12} & d_{13} \\ d_{12} & d_{22} & d_{23} \\ d_{13} & d_{23} & d_{33} \end{bmatrix}$$

$$\Omega_{ij} = \begin{bmatrix} \sqrt{1-d_{11}} & \sqrt{1-d_{12}} & \sqrt{1-d_{13}} \\ \sqrt{1-d_{12}} & \sqrt{1-d_{22}} & \sqrt{1-d_{23}} \\ \sqrt{1-d_{13}} & \sqrt{1-d_{23}} & \sqrt{1-d_{33}} \end{bmatrix}$$

The integrity tensor is written in matrix form as

$$\mathbf{M} = \begin{bmatrix} \Omega_{11}^2 & 0 & 0 & 0 & 0 & 0 \\ 0 & \Omega_{22}^2 & 0 & 0 & 0 & 0 \\ 0 & 0 & \Omega_{33}^2 & 0 & 0 & 0 \\ 0 & 0 & 0 & \Omega_{12}^2 & 0 & 0 \\ 0 & 0 & 0 & 0 & \Omega_{13}^2 & 0 \\ 0 & 0 & 0 & 0 & 0 & \Omega_{23}^2 \end{bmatrix}$$

The coupling of shear and normal damage is likely to be in between these two formulations. Therefore, further investigation into strength penalties for the coupled analysis is needed. See Barbero's formulation for the damage activation function [1].

Assuming energy equivalence between the damaged and effective spaces, the damaged stiffness tensor $C_{ijkl}$ is defined as a function of the undamaged stiffness as

$$C_{ijkl} = M_{ijmn}\bar{C}_{mnpq}M_{pqkl}$$

The damaged (actual or far field) stresses and elastic strains are

$$\sigma_{ij} = C_{ijkl}\varepsilon_{kl}^{e}$$
$$\varepsilon_{ij}^{e} = C_{ijkl}^{-1}\sigma_{kl}$$

and the effective (local) stresses and elastic strains are

$$\bar{\sigma}_{ij} = \bar{C}_{ijkl}\bar{\varepsilon}_{kl}^{e}$$
$$\bar{\varepsilon}_{ij}^{e} = \bar{C}_{ijkl}^{-1}\bar{\sigma}_{kl}$$

Thus, the damaged and effective configurations are related by

$$\sigma_{ij} = M_{ijkl}\bar{\sigma}_{kl}$$
$$\varepsilon_{ij}^{e} = M_{ijkl}^{-1}\bar{\varepsilon}_{kl}^{e}$$

The explicit form of nominal thermodynamic force $Y_{ij}$ is given in terms of effective strain in contracted form as

$$Y_{ij} = \begin{Bmatrix} \frac{1}{\Omega_{11}^2}\left(\bar{C}_{11}\bar{\varepsilon}_1^{e\,2} + \bar{C}_{12}\bar{\varepsilon}_1^e\bar{\varepsilon}_2^e + \bar{C}_{13}\bar{\varepsilon}_1^e\bar{\varepsilon}_3^e\right) \\ \frac{1}{\Omega_{22}^2}\left(\bar{C}_{22}\bar{\varepsilon}_2^{e\,2} + \bar{C}_{12}\bar{\varepsilon}_1^e\bar{\varepsilon}_2^e + \bar{C}_{23}\bar{\varepsilon}_2^e\bar{\varepsilon}_3^e\right) \\ \frac{1}{\Omega_{33}^2}\left(\bar{C}_{33}\bar{\varepsilon}_3^{e\,2} + \bar{C}_{13}\bar{\varepsilon}_1^e\bar{\varepsilon}_3^e + \bar{C}_{23}\bar{\varepsilon}_2^e\bar{\varepsilon}_3^e\right) \\ \frac{1}{\Omega_{44}^2}2\bar{C}_{44}\bar{\varepsilon}_4^{e\,2} \\ \frac{1}{\Omega_{55}^2}2\bar{C}_{55}\bar{\varepsilon}_5^{e\,2} \\ \frac{1}{\Omega_{66}^2}2\bar{C}_{66}\bar{\varepsilon}_6^{e\,2} \end{Bmatrix}$$

for the uncoupled formulation and

$$Y_{ij} = \begin{Bmatrix} \frac{1}{\Omega_{11}^2}\left(\bar{C}_{11}\bar{\varepsilon}_1^{e\,2} + \bar{C}_{12}\bar{\varepsilon}_1^e\bar{\varepsilon}_2^e + \bar{C}_{13}\bar{\varepsilon}_1^e\bar{\varepsilon}_3^e + 2\bar{C}_{44}\bar{\varepsilon}_4^{e\,2} + 2\bar{C}_{55}\bar{\varepsilon}_5^{e\,2}\right) \\ \frac{1}{\Omega_{22}^2}\left(\bar{C}_{22}\bar{\varepsilon}_2^{e\,2} + \bar{C}_{12}\bar{\varepsilon}_1^e\bar{\varepsilon}_2^e + \bar{C}_{23}\bar{\varepsilon}_2^e\bar{\varepsilon}_3^e + 2\bar{C}_{44}\bar{\varepsilon}_4^{e\,2} + 2\bar{C}_{66}\bar{\varepsilon}_6^{e\,2}\right) \\ \frac{1}{\Omega_{33}^2}\left(\bar{C}_{33}\bar{\varepsilon}_3^{e\,2} + \bar{C}_{13}\bar{\varepsilon}_1^e\bar{\varepsilon}_3^e + \bar{C}_{23}\bar{\varepsilon}_2^e\bar{\varepsilon}_3^e + 2\bar{C}_{55}\bar{\varepsilon}_5^{e\,2} + 2\bar{C}_{66}\bar{\varepsilon}_6^{e\,2}\right) \\ 0 \\ 0 \\ 0 \end{Bmatrix}$$

for Barbero's coupled formulation.

The damage surface can be any homogeneous function of the thermodynamic force conjugate to damage. Similarly, the plastic surface and potential functions are given in terms of stress. The classical orthotropic yield criterion of Hill is used [11].

### *2.2.2. Damage and Plastic Evolution*

An associative model where the damage surface and damage potential are identical ($g_d = f_d$) is used to simplify computation. Likewise, the plastic strain surface and potential are made to be identical ($g_p = f_p$). Therefore, the evolution of the internal variables can be described by the following flow rules

$$\dot{D}_{ij} = \dot{\lambda}^d \frac{\partial g_d}{\partial Y_{ij}} \quad ; \quad \dot{\delta} = \dot{\lambda}^d \frac{\partial g_d}{\partial \gamma}$$
$$\dot{\bar{\varepsilon}}_{ij} = \dot{\lambda}^p \frac{\partial g_p}{\partial \bar{\sigma}_{ij}} \quad ; \quad \dot{p} = \dot{\lambda}^d \frac{\partial g_p}{\partial R}$$

## 2.3. Transversely isotropic damage

The following provides the theoretical framework and numerical implementation of a transversely isotropic damage model for use in epoxy impregnated yarns. The formulation is based on [4, 5, 9]; however, the bulk of the theory and implementation is taken from [9]. Damage is tracked transversely and axially with the fibers. Under one dimensional monotonic loading, the principal strain direction corresponds to the primary material direction and the transversely isotropic model is identical to the general orthotropic material in [7]. Refer to [7] for the thermodynamic formulation of the continuous damage model and material parameter identification.

### *2.3.1. Transversely Isotropic Elastic Damage*

In order for this model to be considered for yarn analysis, radius of curvature for a woven yarn must be much less than the fiber diameter.

Micro-cracking in an isotropic or transversely isotropic material occurs in planes determined by the principal strain state [9]. A yarn and some unidirectional lamina can often be considered transversely isotopic. In these cases, the principal axis are assumed in the anisotropic direction and in the isotopic directions where shear strain $\varepsilon_{23} = 0$. The strain in material coordinates is given as $\{\epsilon\} = \{ \epsilon_{11}, \epsilon_{22}, \epsilon_{33}, 2\epsilon_{12}, 2\epsilon_{13}, 2\epsilon_{23}\}^T$. Rotation about the anisotropic axis (1), usually associated with the fiber direction, is accomplished by the strain transformation matrix

$$\{\varepsilon\} = [T]\{\epsilon\}$$

where

$$T = \begin{bmatrix} 1 & 0 & 0 & 0 & 0 & 0 \\ 0 & c^2 & s^2 & 0 & 0 & cs \\ 0 & s^2 & c^2 & 0 & 0 & -cs \\ 0 & 0 & 0 & c & -s & 0 \\ 0 & 0 & 0 & s & c & 0 \\ 0 & -2cs & 2cs & 0 & 0 & c^2 - s^2 \end{bmatrix}$$

and c = cos(θ) and s = sin(θ). The rotation angle θ can be solved by setting $T_{i6}\epsilon_i = 0$.

$$T_{i6}\epsilon_i = 2cs(\epsilon_{33} - \epsilon_{22}) + 2(c^2 - s^2)\,\epsilon_{23} = 0$$

$$\theta = tan^{-1}(2\epsilon_{23} / (\epsilon_{22} - \epsilon_{33}))/2$$

The resultant strain state is given as $\{\varepsilon\} = \{ \varepsilon_{11}, \varepsilon_{22}, \varepsilon_{33}, \varepsilon_{12}, \varepsilon_{13}, 0\}^T$.

The material maintains transverse isotropy when in-plane stresses are either both tensile or both compressive. However, since damage effects are different in tension and compression, if the damaging in-plane principal stresses are opposite sign, the material becomes orthotropic. The

axis of in-plane anisotropy will always correspond to the principal axis. Thus, tensile and compressive damage are isotropic in the transverse plane. This relationship is expressed in the damage variables defined as

$$d_1 = d_L \frac{\langle \sigma_{11} \rangle}{|\sigma_{11}|} + c_L d_L \frac{\langle -\sigma_{11} \rangle}{|\sigma_{11}|}$$

$$d_2 = d_T \frac{\langle \sigma_{22} \rangle}{|\sigma_{22}|} + c_T d_T \frac{\langle -\sigma_{22} \rangle}{|\sigma_{22}|}$$

$$d_3 = d_T \frac{\langle \sigma_{33} \rangle}{|\sigma_{33}|} + c_T d_T \frac{\langle -\sigma_{33} \rangle}{|\sigma_{33}|}$$

where $c_L$ and $c_T$ are the longitudinal and transverse crack closure coefficients.

Where longitudinal and transverse integrity are written as

$$\Omega_{11} = 1 - d_1$$

$$\Omega_{22} = 1 - d_2$$

$$\Omega_{33} = 1 - d_3$$

Since shear integrity is a function of both in and out-of-plane damage, and assuming shear damaged is isotropic, the resulting integrities are given as.

$$\Omega_{12} = \Omega_{13} = \sqrt{(1 - c_S d_T)(1 - c_S d_L)}$$

where $c_S$ is the shear crack closure coefficient.

The undamaged compliance tensor in the material/principal direction is given as

$$\bar{S} = \begin{bmatrix} \frac{1}{E_1} & -\frac{\nu_{21}}{E_2} & -\frac{\nu_{21}}{E_2} & 0 & 0 & 0 \\ -\frac{\nu_{12}}{E_1} & \frac{1}{E_2} & -\frac{\nu_{23}}{E_3} & 0 & 0 & 0 \\ -\frac{\nu_{12}}{E_1} & -\frac{\nu_{23}}{E_2} & \frac{1}{E_2} & 0 & 0 & 0 \\ 0 & 0 & 0 & \frac{1}{G_{12}} & 0 & 0 \\ 0 & 0 & 0 & 0 & \frac{1}{G_{12}} & 0 \\ 0 & 0 & 0 & 0 & 0 & \frac{1}{G_{23}} \end{bmatrix}$$

The undamaged stiffness tensor is given as

$$\overline{C} = \overline{S}^{-1}$$

### *2.3.2. Thermodynamic Formulation*

The following stresses and thermodynamic forces are defined as functions of the Helmholtz free energy density $\psi$

$$\sigma_{ij} = \rho \frac{\partial \psi}{\partial \varepsilon_{ij}} = C_{ijkl}\varepsilon_{kl}$$

$$Y_{ij} = \rho \frac{\partial \psi}{\partial D_{ij}} = -\frac{1}{2}\varepsilon_{kl}\frac{\partial C_{klpq}}{\partial D_{ij}}\varepsilon_{pq}$$

Depending on the loading condition the thermodynamic forces takes on different forms. The explicit form of the thermodynamic force $Y_{ij}$ is given in terms of effective strain in contracted form as

$$Y_{ij} = \begin{Bmatrix} \frac{1}{1-d_L}(\bar{C}_{11}\bar{\varepsilon}_1^2 + \bar{C}_{12}\bar{\varepsilon}_1\bar{\varepsilon}_2 + \bar{C}_{13}\bar{\varepsilon}_1\bar{\varepsilon}_3) + \frac{2c_S}{1-c_S d_L}(\bar{C}_{44}\bar{\varepsilon}_4^2 + \bar{C}_{55}\bar{\varepsilon}_5^2) \\ \frac{1}{1-d_T}(\bar{C}_{22}\bar{\varepsilon}_2^2 + \bar{C}_{12}\bar{\varepsilon}_1\bar{\varepsilon}_2 + \bar{C}_{23}\bar{\varepsilon}_2\bar{\varepsilon}_3) + \frac{2c_S}{1-c_S d_T}\bar{C}_{44}\bar{\varepsilon}_4^2 \\ \frac{1}{1-d_T}(\bar{C}_{33}\bar{\varepsilon}_3^2 + \bar{C}_{13}\bar{\varepsilon}_1\bar{\varepsilon}_3 + \bar{C}_{23}\bar{\varepsilon}_2\bar{\varepsilon}_3) + \frac{2c_S}{1-c_S d_T}\bar{C}_{55}\bar{\varepsilon}_5^2 \\ 0 \\ 0 \\ 0 \end{Bmatrix}$$

and compressive loading

$$Y_{ij} = \begin{Bmatrix} \frac{c_L}{1-c_L d_L}(\bar{C}_{11}\bar{\varepsilon}_1^2 + \bar{C}_{12}\bar{\varepsilon}_1\bar{\varepsilon}_2 + \bar{C}_{13}\bar{\varepsilon}_1\bar{\varepsilon}_3) + \frac{2c_S}{1-c_S d_L}(\bar{C}_{44}\bar{\varepsilon}_4^2 + \bar{C}_{55}\bar{\varepsilon}_5^2) \\ \frac{c_T}{1-c_T d_T}(\bar{C}_{22}\bar{\varepsilon}_2^2 + \bar{C}_{12}\bar{\varepsilon}_1\bar{\varepsilon}_2 + \bar{C}_{23}\bar{\varepsilon}_2\bar{\varepsilon}_3) + \frac{2c_S}{1-c_S d_T}\bar{C}_{44}\bar{\varepsilon}_4^2 \\ \frac{c_T}{1-c_T d_T}(\bar{C}_{33}\bar{\varepsilon}_3^2 + \bar{C}_{13}\bar{\varepsilon}_1\bar{\varepsilon}_3 + \bar{C}_{23}\bar{\varepsilon}_2\bar{\varepsilon}_3) + \frac{2c_S}{1-c_S d_T}\bar{C}_{55}\bar{\varepsilon}_5^2 \\ 0 \\ 0 \\ 0 \end{Bmatrix}$$

A thermodynamically consistent model is implemented by defining the transverse damage activation function as

$$g_T = (J_{22}Y_2^2 + J_{33}Y_3^2)^{1/2} - (\gamma_T(\delta) - \gamma_{To})$$

where

$$\gamma_T(\delta_T) = \sum_{i=1}^{n} \alpha_{Ti}\left[exp\left(\frac{\delta_T}{\beta_{Ti}}\right) - 1\right]$$

The associated transverse damage and evolution the terms evolve as

$$\dot{d}_T = \max_{i,j=2,3}\left[\dot{\lambda}\frac{\partial g_T}{\partial Y_{ij}}\right]$$

$$\dot{\delta}_T = \dot{\lambda}\frac{\partial g_T}{\partial \gamma_T}$$

The longitudinal damage activation is defined for both tension and compression as

$$g_L = (J_{11}Y_1^2)^{1/2} - (\gamma_L(\delta) - \gamma_{Lo})$$

$$\gamma_L(\delta_T) = \sum_{i=1}^{n} \alpha_{Li}\left[exp\left(\frac{\delta_{L\pm}}{\beta_{Li}}\right) - 1\right]$$

$$\delta_{L\pm} = \delta_{L+}\frac{\langle\sigma_{11}\rangle}{|\sigma_{11}|} + \delta_{L-}\frac{\langle-\sigma_{11}\rangle}{|\sigma_{11}|}$$

and the damage evolution term is forced to evolve separately for tension and compression. For associated damage evolution the term evolves as

For tensile loads: $\dot{\delta}_{L+} = \dot{\lambda}\frac{\partial g_L}{\partial \gamma_L}$ and $\dot{\delta}_{L-} = 0$

For compressive loads: $\dot{\delta}_{L-} = \dot{\lambda}\frac{\partial g_L}{\partial \gamma_L}$ and $\dot{\delta}_{L+} = \begin{cases} \dot{\lambda}\frac{\partial g_L}{\partial \gamma_L} & for\ \ \delta_{L+} \geq \delta_{L-} \\ 0 & for\ \ \delta_{L+} < \delta_{L-} \end{cases}$

and the longitudinal damage as

$$\dot{d}_L = \dot{\lambda}\frac{\partial g_L}{\partial Y_{11}}$$

Thus, the tensile damage surface evolves for both compression and tension loads while the compressive term only evolves for compression loads.

## 2.4. Micro-macro damage

Micromechanics can be used to isolate the damage evolution in the constituents (fiber and matrix). Given statistically accurate stress and strain concentration tensors, constituent damage can be predicted using the methodology in [8]. The following section outlines the proposed material model. While this approach was originally favored instead of a phenomenological approach, it is not entirely clear how the interphase damage portion used in calibration influences the constituent damage evolution. The interphase is a finite chemically different transition region between the fiber and matrix. Since a complete verification and validation of this model is not provided, the approach was not used in multiscale analysis. However, the theory and implementation is useful and various future works are garnered.

### *2.4.1. Outline of constitutive equation*

1. The stress/strain concentration tensors live in the effective configuration. First, calculate effective volume fractions.

$$\bar{V}^f = \frac{V^f\left(1 - D_{eq}^f\right)}{V^f\left(1 - D_{eq}^f\right) + V^m\left(1 - D_{eq}^m\right)}$$

$$\bar{V}^m = \frac{V^m\left(1 - D_{eq}^m\right)}{V^f\left(1 - D_{eq}^f\right) + V^m\left(1 - D_{eq}^m\right)}$$

where equivalent damage is

$$D_{eq}^f = \left(D_{11}^{f\,2} + D_{22}^{f\,2} + D_{33}^{f\,2}\right)^{1/2}$$

$$D_{eq}^m = (D_{11}^{m\,2} + D_{22}^{m\,2} + D_{33}^{m\,2})^{1/2}$$

and the superscripts *f*, *m* and later *L* correspond to fiber, matrix and interphase respectively.

2. Using Appendix B of [1], calculate the strain concentration tensors in the effective configuration

$$\bar{A}_{ijkl}^f = \left(\bar{C}_{ijrs}^m - \bar{C}_{ijrs}^f\right)^{-1}\left[\left(\bar{C}_{rskl}^m - \bar{C}_{rskl}^f\right)^{-1} - P_{rskl}\right]^{-1}$$

$$\bar{A}_{ijkl}^m = \frac{1}{1 - \bar{V}^f}\left(I_{ijkl} - \bar{V}^f \bar{A}_{ijkl}^f\right)$$

where $\bar{C}$ are the undamaged stiffness tensor of the constituents and $P_{rskl}$ account for the microstructural geometry. The effective homogenized stiffness tensor is then

$$\bar{C}_{ijkl} = \bar{V}^f \bar{C}^f_{ijrs} \bar{A}^f_{rskl} + \bar{V}^m \bar{C}^m_{ijrs} \bar{A}^m_{rskl}$$

3. Using the current damage effects tensor, calculate the strain concentration tensor in the partially damaged configuration

$$\tilde{A}^f = [V^m [M^m]^{-1} \bar{A}^m \bar{A}^{f-1} [M^f]^{-1} + V^f I]^{-1}$$

$$\tilde{A}^m = \frac{1}{V^m} \left[ I - V^f \tilde{A}^f \right]$$

4. Since interphase damage is said not to affect the volume fraction, the stiffness in the partially damaged configuration is

$$\tilde{C}_{ijkl} = V^f \tilde{C}^f_{ijrs} \tilde{A}^f_{rskl} + V^m \tilde{C}^m_{ijrs} \tilde{A}^m_{rskl}$$

5. Similarly, the fully damaged stiffness tensor is then

$$C_{ijrs} = \left[ M^L_{ijkl} \right]^{-1} \tilde{C}_{klmn} [M^L_{mnrs}]^{-1}$$

6. Calculate initial partially damaged strain using the current interphase damage effects tensor

$$\tilde{\varepsilon}_{ij} = \left[ M^L_{ijkl} \right]^{-1} \varepsilon_{kl}$$

7. Using the strain concentration tensors, calculate the strain in the in the partially damaged configuration

$$\tilde{\varepsilon}^f_{ij} = \tilde{A}^f_{ijkl} \tilde{\varepsilon}_{kl}$$
$$\tilde{\varepsilon}^{\mathrm{m}}_{\mathrm{ij}} = \tilde{\mathrm{A}}^{\mathrm{m}}_{\mathrm{ijkl}} \tilde{\varepsilon}_{\mathrm{kl}}$$

8. Using the constituent damage tensors, calculate the strain in the in the effective configuration

$$\bar{\varepsilon}^f_{ij} = \left[ M^f_{ijkl} \right]^{-1} \tilde{\varepsilon}^f_{kl}$$
$$\bar{\varepsilon}^m_{ij} = \left[ M^m_{ijkl} \right]^{-1} \tilde{\varepsilon}^m_{kl}$$

9. For each of the constituents, continuum damage mechanics is used to calculate stiffness loss.

### *2.4.2. Constitutive Decomposition*

The stress and strain concentration tensors $B_{ijkl}$ and $A_{ijkl}$ are calculated using micromechanics such that the constituent stress terms are related to stress in the homogenized material as

$$\sigma_{ij}^{r} = B_{ijkl}^{r}\sigma_{kl} \quad ; \quad B_{ijkl}^{r} = C_{ijrs}^{r}A_{rsuv}^{r}C_{uvkl}^{-1}$$

$$\varepsilon_{ij}^{r} = A_{ijkl}^{r}\varepsilon_{kl} \quad ; \quad A_{ijkl}^{r} = C_{ijrs}^{r-1}B_{rsuv}^{r}C_{uvkl}$$

where $r = f, m, L$ for fiber, matrix and interphase respectively.
Assuming the yarn is composed of long circular cylindrical fibers; the strain concentration factor is given by

$$A_{ijkl}^{f} = \left(C_{ijrs}^{m} - C_{ijrs}^{f}\right)^{-1}\left[\left(C_{rskl}^{m} - C_{rskl}^{f}\right)^{-1} - P_{rskl}\right]^{-1}$$

$$A_{ijkl}^{m} = \frac{1}{1 - V^{f}}\left(I_{ijkl} - V^{f}A_{ijkl}^{f}\right)$$

where the components of the symmetric geometry tensor $P_{ijkl}$ is given in [1].

For fiber, matrix and interphase there exists an independent damage effects tensor ($M^f$, $M^m$, $M^L$). The total damage effects tensor is given by

$$M_{ijkl} = \left(V^{f}M_{ijkl}^{f}B_{kluv}^{f} + V^{m}M_{ijkl}^{m}B_{kluv}^{m}\right)M_{uvrs}^{L}$$

where $V^f$ and $V^m$ are the fiber and matrix volume fractions respectively and

The strain concentration tensors are given in the partially damaged configuration as

$$\tilde{A}^{f} = [V^{m}M^{m-1}\bar{A}^{m}\bar{A}^{f-1}M^{f-1} + V^{f}I]^{-1}$$
$$\tilde{A}^{m} = \frac{1}{V^{m}}\left[I - V^{f}\tilde{A}^{f}\right]$$

The effective volume fraction in the effective configuration is given as

$$\bar{V}^{r} = \frac{V^{r}\left(1 - D_{eq}^{r}\right)}{V^{f}\left(1 - D_{eq}^{f}\right) + V^{m}\left(1 - D_{eq}^{m}\right)}$$

where equivalent damage is given as the sum of the squares of the damage components or

$$D_{eq}^{r} = (D_{11}^{r\,2} + D_{22}^{r\,2} + D_{33}^{r\,2})^{1/2}$$

### *2.4.3. Integration Scheme*

Update current strain value

$$\left(\varepsilon_{ij}\right)^{n} = \left(\varepsilon_{ij}\right)^{n-1} + \left(\Delta\varepsilon_{ij}\right)^{n}$$

Initialize state variables with values from previous step (9 total)

$$\left(D_{ij}^{m}\right)^{n} = \left(D_{ij}^{m}\right)^{n-1} \quad ; \quad (\delta^{m})^{n} = (\delta^{m})^{n-1}$$

$$\left(D_{ij}^{f}\right)^{n} = \left(D_{ij}^{f}\right)^{n-1} \quad ; \quad (\delta^{f})^{n} = (\delta^{f})^{n-1}$$

$$\left(D_{ij}^{L}\right)^{n} = \left(D_{ij}^{L}\right)^{n-1} \quad ; \quad (\delta^{L})^{n} = (\delta^{L})^{n-1}$$

Calculate the effective strain with updated damage effects tensor

$$\tilde{\varepsilon}_{ij} = M_{ijkl}^{L-1}\varepsilon_{kl}^{m}$$

Calculate the partially damaged strain concentration factors using updated effective volume fraction and strain concentration factors

$$\tilde{A}^{f} = [V^{m}M^{m-1}\bar{A}^{m}\bar{A}^{f-1}M^{f-1} + V^{f}I]^{-1}$$

$$\tilde{A}^{m} = \frac{1}{V^{m}}\left[I - V^{f}\tilde{A}^{f}\right]$$

Then calculate the effective strain and strain in the constituents

$$\varepsilon_{ij}^{r} = M_{ijkl}^{r-1}\tilde{A}_{klrs}^{r}\tilde{\varepsilon}_{rs}$$

$$\bar{\sigma}_{ij}^{r} = \bar{C}_{ijkl}^{r}\bar{\varepsilon}_{kl}^{r}$$

Use the effective stress to determine compression or tension. If compression; recalculate the damaged effects tensor with crack closure coefficients and then repeat steps to calculated effective strain in the constituents and total partially damaged strain.

Calculate the partially damage stiffness tensors as

$$\tilde{C}_{ijkl}^{r} = M_{ijmn}^{r-1}\bar{C}_{mnpq}^{r}M_{pqkl}^{r-1}$$

$$\tilde{C}_{ijkl} = V_{0}^{f}\tilde{A}_{ijkl}^{f}\tilde{C}_{ijkl}^{f} + V_{0}^{m}\tilde{A}_{ijkl}^{m}\tilde{C}_{ijkl}^{m}$$

where $V_o$ is the initial volume fraction.

Calculate the thermodynamic forces and damage hardening function in terms of effective strain and stiffness for the fiber and matrix and total partially damaged strain and stiffness for the interphase.

$$\gamma^r = \sum_{i=1}^{n} \alpha_i^r \left[ exp\left(\frac{\delta^r}{\beta_i^r}\right) - 1 \right]$$

$$g^r = \sqrt{Y_{ij}^r J_{ijkl}^r Y_{kl}^r} + \sqrt{\left|H_{ij}^r Y_{ij}^r\right|} - (\gamma^r + \gamma_o^r)$$

Check for damage: if $g^r > 0$ damage occurs; iterate until $\Delta\lambda^m \approx 0$ ($g^m \approx 0$). If damage occurs in one of the constituents, update its state variables using the following scheme.

Using a first order linearized scheme for the k$^{th}$ iteration; the damage multiplier is found from

$$(g^r)_k - (g^r)_{k-1} = \left(\frac{\partial g^r}{\partial Y^r}\frac{\partial Y^r}{\partial D^r}\frac{\partial f^r}{\partial Y^r} + \frac{\partial \gamma^r}{\partial \delta^r}\right)_{k-1} \Delta\lambda_k^r = 0$$

where the non-associated damage potential is given as

$$f^m = \sqrt{Y_{ij}^m J_{ijkl}^m Y_{kl}^m} - (\gamma^m + \gamma_o^m)$$

thus

$$\Delta\lambda_k^r = -(g^r)_{k-1} \left(\frac{\partial g^r}{\partial Y^r}\frac{\partial Y^r}{\partial D^r}\frac{\partial f^r}{\partial Y^r} + \frac{\partial \gamma^r}{\partial \delta^r}\right)_{k-1}^{-1} = 0$$

Update damage state variable for next iteration

$$\left(D_{ij}^r\right)_k^n = \left(D_{ij}^r\right)_{k-1}^n + \Delta\lambda_k^r \left(\frac{\partial f^r}{\partial Y^r}\right)_{k-1}$$

$$(\delta^r)_k^n = (\delta^r)_{k-1}^n + \Delta\lambda_k^r \left(\frac{\partial f^r}{\partial \gamma^r}\right)_{k-1} = (\delta^r)_{k-1}^n - \Delta\lambda_k^r$$

Calculate the fully damaged stiffness tensor and stress components and update state variables

$$C_{ijkl} = M_{ijpq}^{L-1} \tilde{C}_{pqrs} M_{rskl}^{L-1}$$

$$\sigma_{ij} = C_{ijkl}\varepsilon_{ij}$$

## 2.5. Crack Band Theory

A useful addition to the above mentioned material models is the use of crack band theory to model the post failure softening behavior [12]. This method can be implemented in order to simulate the fracture process in a yarn. The general orthotropic formulation uses softening parameters to modify the integrity values post failure. Continuum damage mechanics can be assumed up to first failure. Then the remaining fracture energy is dissipated through softening.

For many unidirectional materials (yarns), linear elastic to failure is a good approximation. For this study, only the elastic crack band model is implemented.

Bazant and Oh [12] proposed damage based relationship for a failed material undergoing linear strain softening. Using the damaged stiffness tensor from section 2.2.1, the integrity components are evolved post fracture (strain-localization) as a function of the normal (crack-opening) strain component.

$$\Omega_{11}^2 = \frac{E_t(\varepsilon_o - \varepsilon_{11})}{E_{11}\varepsilon_{11}}$$

Where $E_t$ it the negative tangent modulus of the linear softening portion, $\varepsilon_o$ is the total strain at the end of strain-softening and $E_{11}$ is the modulus at the end of continuum damage evolution (distributed cracks). $E_t$ can be determined by the required strain energy density absorbed through the fracture process, which is directly related to the surface energy generated due to fracture. Therefore, the characteristic length of the element ($l^*$ = element size) [4, 5] and fracture toughness ($G_f$) of the material are used to determine the total energy density at failure as

$$W = \frac{G_f}{l^*}$$

with the constraint that

$$W = \int \sigma_{11} d\varepsilon_{11}$$

for unidirectional loading. $E_t$ is calculated based on a linear stress verses strain decay. A more complete description of these parameters is given in the aforementioned references.

Strain localization using implicit analysis, requires special controls on the element failure selection. Sierra's control failure methodology described in [13] is invoked with one modification. This methodology assumes that exceeding one failure mechanism results in a decay of all the stress components. This implementation only decays the stresses related to the orthotropic plane in which failure occurred. This means full "element death" only occurs when all three planes have failed. This allows for fiber connectivity with transverse failure. Unfortunately, this means the control failure methodology only works for the first failure mode. This is an appropriate approximation when simple loadings only result in one failure mode, but may induce unrealistic failure clouds in secondary modes.

The following provides a mesh convergence verification example. An elliptically notched plate ($a/b$ = 4) is loaded to failure. The material is a glass fiber composite with a transverse stiffness of $E_{22}$ = 16.8 GPa, a peak stress of $f_2$ = 41 MPa and a critical energy release rate of $G_I$ = 0.50 MPa-mm. Four mesh sizes are implemented in implicit analysis. These require four transverse material responses shown in Figure 1. The peak load from each simulation is shown in Figure 2. Mesh convergence is assured however is achieved slowly.

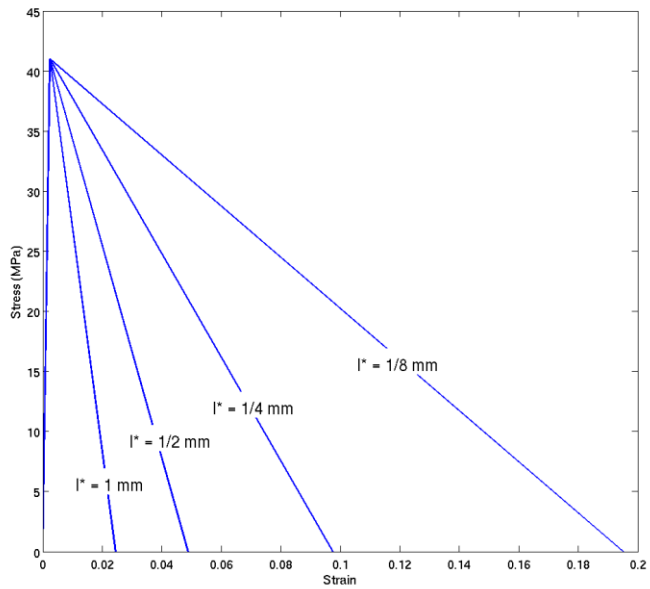


Figure 1. Tensile stress-strain relationships for various characteristic lengths.

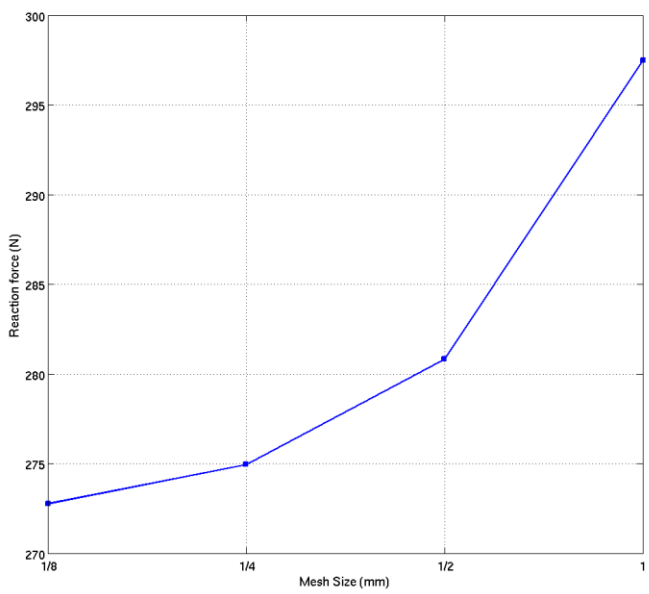


Figure 2. Mesh convergence results: peak load versus mesh size for an elliptically notched plate under tension.

## 2.6. Polymer Matrix

It is assumed that the matrix material can be modeled as homogeneous and any void content is not modeled explicitly rather is included in the constitutive response. Thus the matrix is approximated as Isotropic $J_2$ plastic.

The multi-linear elastic plastic failure model is used to simulate crack initiation and growth in both micro and meso-mechanical simulations. The parameters for post failure softening are estimated from [14]. Figure 3 shows the stress strain relationship assumed for the UF3362-100 resin material based on manufacturer's specifications for a mesh size.

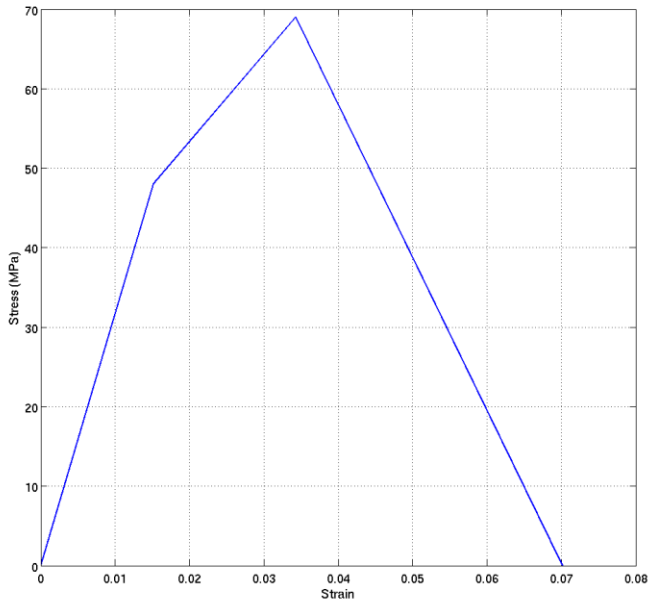


Figure 3. Estimated stress-strain relationship for UF3362-100 cured resin.

# 3. EXPERIMENTAL RESULTS

In order to validate finite element simulations, a series of quasi-static tensile experiments have been performed. In addition, edge and surface microscopy images have been investigated in order to accurately depict fiber bundle morphology and damage nucleation and growth behavior.

## 3.1. Materials

The glass fiber reinforced polymer (GFRP) material used for this investigation is a thermosetting polymer prepreg system with a total fiber volume fraction of approximately 48%. The fiber architecture is an eight-harness satin weave composed of E-glass fibers of 6 µm in diameter. A representative unit cell of a post-mortem fractured surface for this architecture is shown in Figure 4.

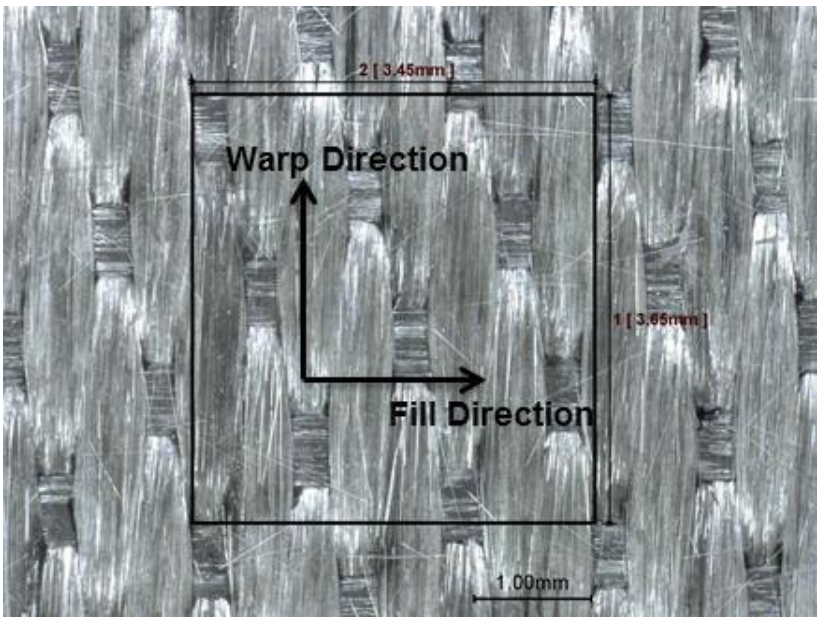


Figure 4. GFRP 8-harness satin weave fiber surface with a unit cell illustrated. Warp face is shown with the warp direction vertically oriented.

## 3.2. Specimen Processing

Prepreg laminates have been hand laid from individual plies cut using a 4-axis CNC flatbed cutter. Panels (250 mm x 300 mm) composed of 6 plies have been laid up in a symmetric stack sequence with the warp face of each ply facing out away from the mid-thickness plane, and the warp direction oriented along the tensile loading direction. Panels were vacuumed bagged and autoclave cured according to the manufacturer's recommendations. Beveled end tabs were then secondarily bonded to consolidated panels and specimens were cut using a wet saw equipped with a diamond embedded blade. Resulting specimen geometry can be seen in Figure 5, with the warp fiber direction being collinear with the specimen length.

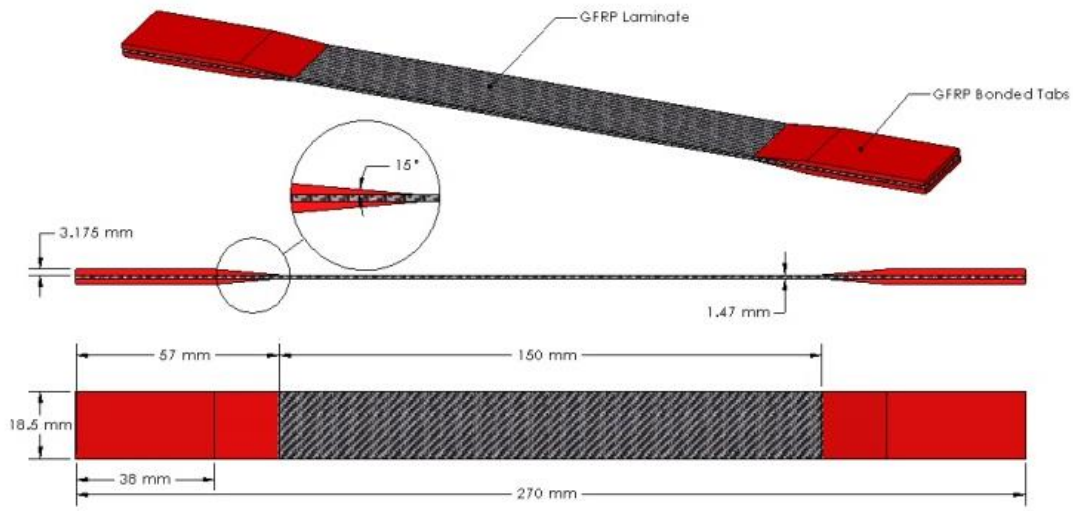


Figure 5. Tensile testing specimen geometry

## 3.3. Testing Procedure

Edge and surface optical microscopy has been performed in order to describe the geometric quantities and spatial distribution necessary to have accuracy in simulation efforts. Monotonic tensile testing in displacement control has then been performed at a displacement rate of 3 mm/min. Strain gage-based extensometers have been utilized to directly measure the axial and transverse strains. The gage lengths for the axial and transverse strain determination were 25.4 mm and 18.5 mm, respectively. Specimens were loaded to failure with load and strain data continually recorded at 10 Hz. Post mortem microscopy was then performed on specimen edges as well as the surfaces in order to correlate with model predictions.

## 3.4. Experimental Results

Edge and surface microscopy images have allowed the direct measurements of tow width, height, spacing and undulation frequency. The resulting morphology has been directly used for modeling input to reconstruct the geometry. A typical front edge micrograph can be seen in Figure 6.

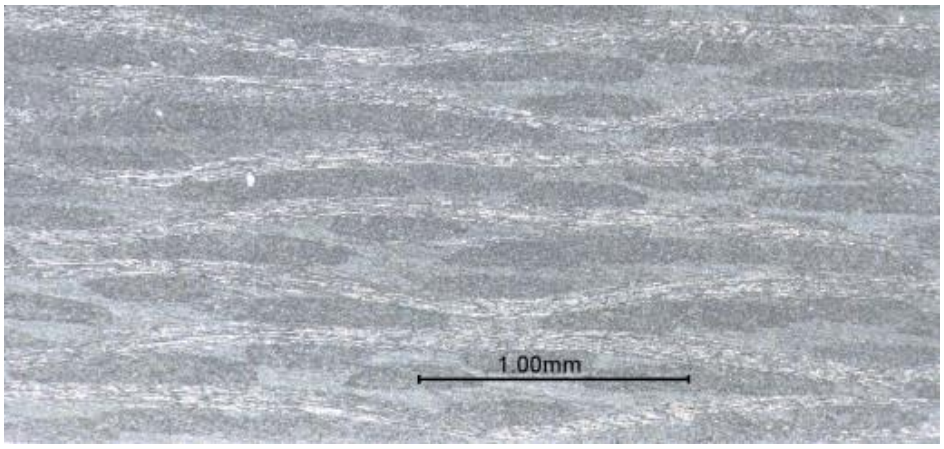


Figure 6. Front edge micrograph detailing warp fiber tow ends

The in-plane unit cell geometry, as shown in Figure 6 for a subsurface post-mortem ply, as well as from the top surface of a cured part in Figure 7, give an idea of the fiber tow packing density. From these images, the average warp and weft yarn count is 23/cm and 22/cm, respectively.

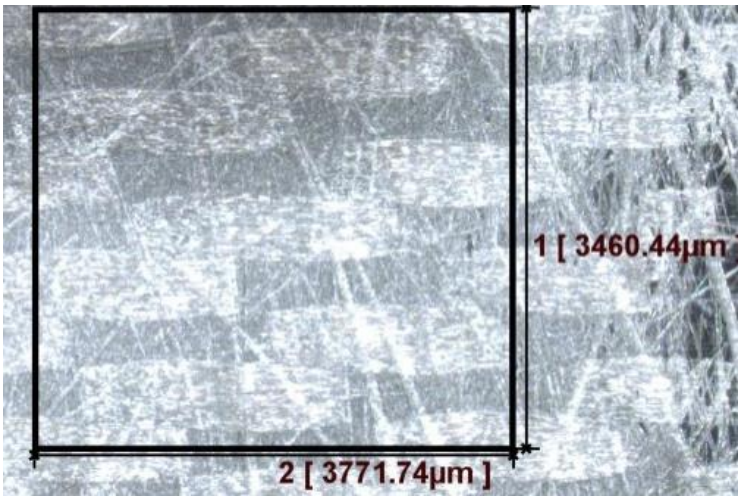


Figure 7. Unit cell from the top surface of an as-cured laminate

When a laminate with various fiber direction angles is loaded in tension, the respective failure of the constituent plies occurs successively in the increasing order of strength [15]. For this particular 8-harness satin weave loaded in tension along the warp fibers, the weft fibers are oriented at 90 degrees to the loading direction. This loading will give rise to transverse cracking within the weft tows. Modulus decreases by approximately 46% at a strain of 0.36%. The modulus then increases by approximately 18% before decaying further as damage progresses. The knee behavior in the stress-strain relationship is shown in Figure 8.

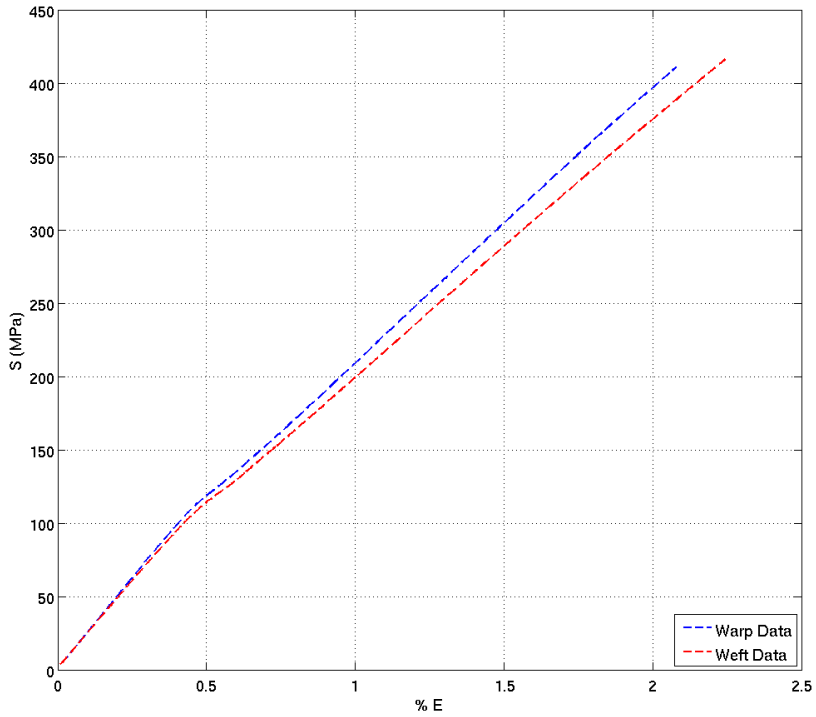


Figure 8. Tensile stress-strain curves for the warp and weft directions of a GFRP

## 3.5. Experimental Requirements

Sufficiently accurate, micro and meso-scale geometries can be generated with minimal insight into the actual structure. However, with more measurements comes higher fidelity and greater statistical representation of the structure. For instance, the geometry for a micromechanical simulation can be generated from no more than the fiber volume fraction. Similarly, a meso-scale geometry needs only total fiber volume, yarn counts and lamina thickness.

Depending on the curing technique, a fiber volume fraction for a woven PMC may be estimated from the manufacturing specification of the prepreg. However, this may not be accurate if substantial polymer is drawn from the prepreg during curing from variations in vacuum pressure and layup. For example, Figure 9 shows two uniaxial tensile experiments for nearly identical 8HS GFRP laminates. The lower curve is more representative of the original prepreg fiber volume fraction (Figure 10), while the upper curve indicates substantial polymer bleeding. The latter would require calibration or direct measurement to determine the actual volume fraction.

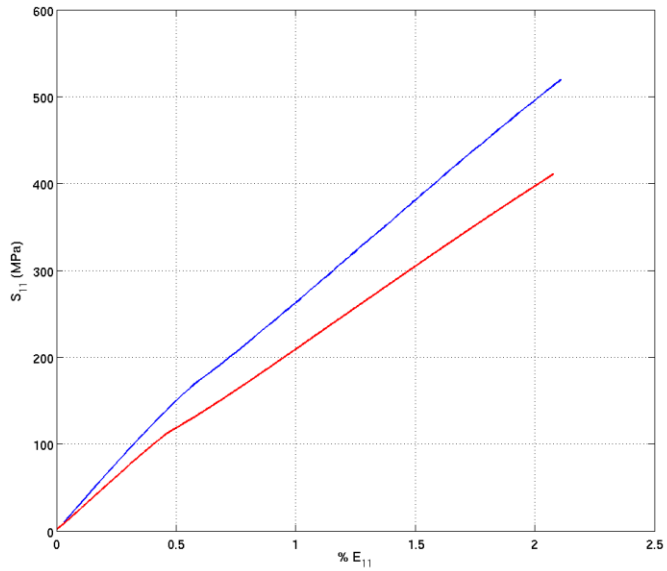


Figure 9. Tensile warp stress-strain curves two GFRP with different manufacturing techniques (data from Wei-Yang Lu)

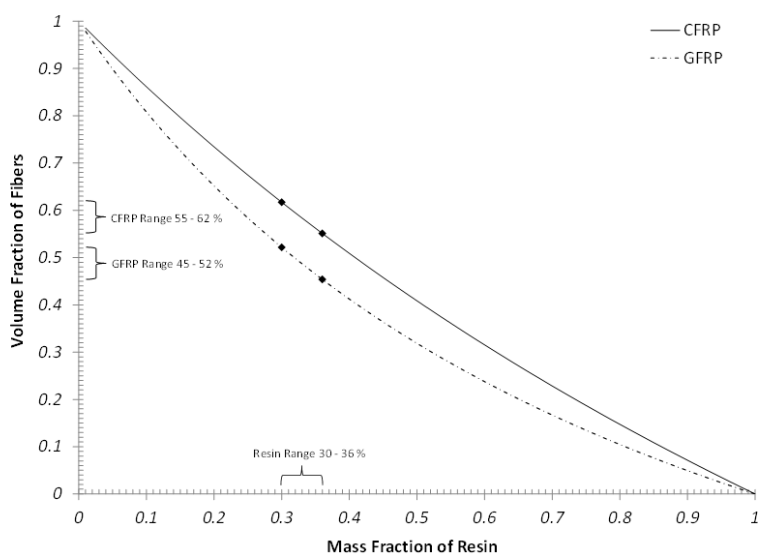


Figure 10. Fiber volume fraction versus resin mass fraction for GFRP and CFRP

# 4. MESH GENERATION

## 4.1. Micromechanical

A representative volume element of the yarn microstructure consists of matrix material and a random arrangement of fibers. Much work has been done by characterizing material response using a structured (hexagonal, square …) fiber packing resulting in a simple unit cell [8, 16-19]. While this structure produces reasonable results under elastic loading, the results produce significant over predictions of strength and damage resistance. Therefore, a random distribution is necessary to accurately predict crack initiation and propagation [20-24].

When placing random disks in a 2D space, a simple random "dart throw" technique can only produce volume fractions on the order of 50%. This packing does not represent the physical process of packing fibers and therefore the volume fractions seen in yarns (60-70%). Another complication in unit-cell generation is the necessity for periodicity. This means the parallel faces of the unit-cell must have identical topology allowing for repeats only through translation. Through collaboration with Dr. Ebeida of Sandia, a periodic maximal Poisson sampling with adaptive disk insertion with a dial-in volume fraction is used to generate the unit cells for this analysis.

Figure 11 shows a representative element loaded transverse to the fibers. The boundary conditions of this simulation are calculated using a multi-scale RVE region. Figure 12 provides examples of the first order homogenized responses of various distributions for a fiber volume fraction of 67%. While the crack path and failure are of qualitative interest; after peak load the model begins to bifurcate and the RVE assumptions become invalid [25]. Therefore, the random fiber-matrix micromechanical simulations will provide estimates of peak stress and not softening behavior. Crack band theory is discussed in section 2.5.

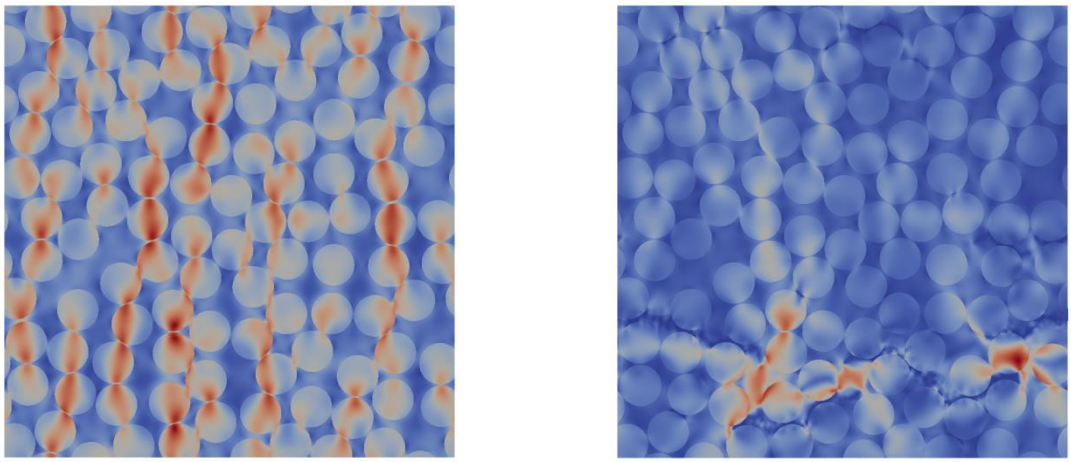

a. b.

Figure 11. RVE von Mises stress distribution under uniaxial transverse tension, a) peak load and b) post fracture

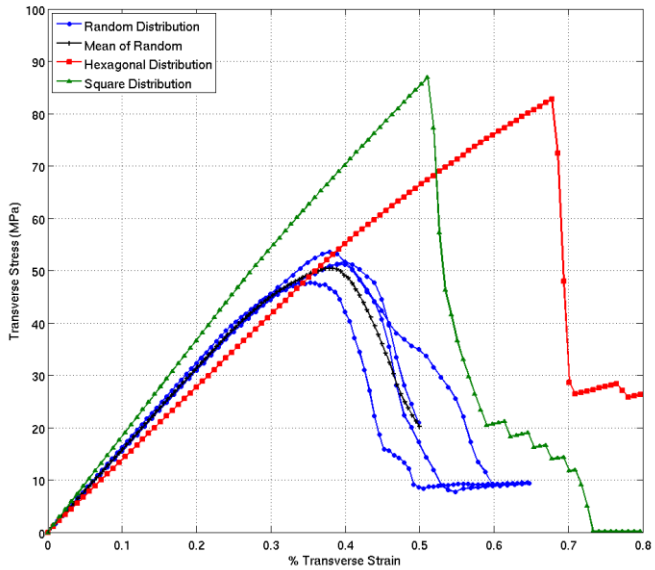


Figure 12. Homogenized tensile response for multiple samplings with a coarse mesh at $v_f = 67\%$

For the micromechanical simulation, the size of the RVE (number of fibers) affects the response. Three randomly generated RVEs with sequentially increasing RVE edge length to fiber radius ratios of 10.9 (least fibers), 21.7 and 43.4 (most fibers) are used to address size sensitivities. Figure 13 shows excellent convergence of the transverse elastic modulus. Near peak load, the RVE method proved problematic for the very large mesh sizes. Therefore, peak load estimates are taken from a plane strain simulation. The peak stresses for the low, medium and high fiber count models are 40.7, 41.1 and 37.8 MPa respectively. These values are similar to those in the mesh convergence study, but without a numerically intensive study into the variation between different realizations, the values cannot be fully verified. However, one would expect the scatter between realizations of each size to reduce with increasing number of fibers. This is demonstrated in [26]. Given the limitations in the time and access to the code, this reference is the only verification given here.

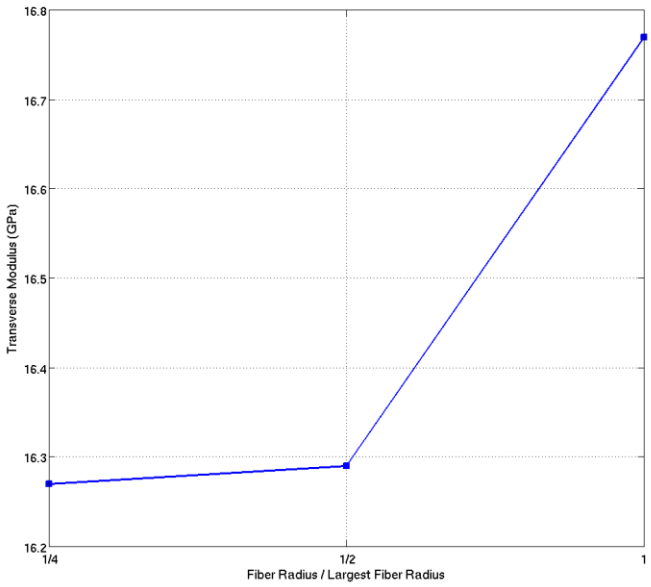


Figure 13. RVE size convergence of transverse modulus for random fiber composites

Bazant shows that localization/softening RVE models are not valid for multi-scale modeling of macro-scale structures without an association of material characteristic length and fracture energy [25]. It should be noted however, that the simulations presented in this study are not associated with a macro-scale structure. Alternatively, the multi-scale RVE approach is simply leveraged to apply realistic boundary conditions. Nevertheless, since the boundary conditions used for a periodic structure with strain localization are questionable, these models are said to produce quantitatively accurate results up to peak load and qualitative insight into the fracture processes during macroscopic softening. Calibration is completed by first simulating the effects distributed cracks and yielding up to peak load, then using the macro/mesoscopic fracture energy to simulate softening. Figure 14 demonstrates the proposed technique. Size effects, or the dependency of the RVE on physical dimensions [16], are not included in this study.

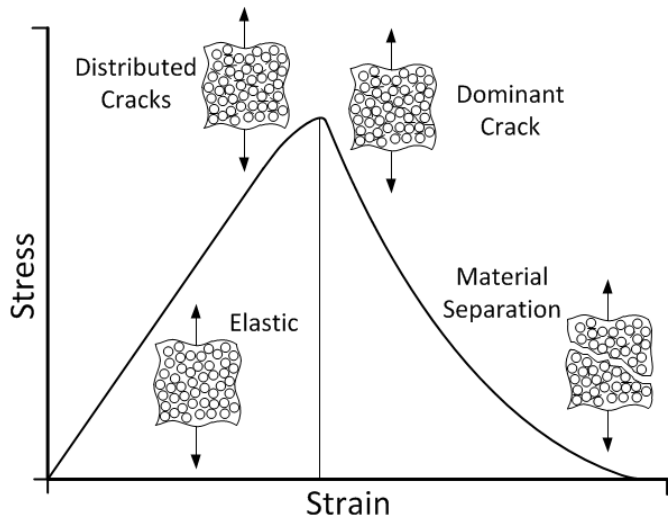

Figure 14. Illustration of the stages of crack development in the constitutive model

These models justify that elastic to failure methodology with crack band type softening is a good approximation for the unidirectional yarn material. The interphase around the fiber is assumed to be made up of matrix material. It is also shown that the peak homogenized stress is insensitive to toughness (energy dissipated with crack band theory) of the interphase [22].

## 4.2. Mesomechanical

The three dimensional geometry of a woven composite on the meso-scale for numerical analysis must be representative of the average true structure and contain certain approximations/assumptions that ease the meshing process. The mesh for simulation is contiguous. Overlapping yarn surfaces are self-similar and do not have a polymer layer of separation. These are instead modeled with cohesive surface elements. Due to the conservation of fibers, the yarn cross-sectional area is more or less constant over the sweep path. Since the sweep cross-section naturally changes along the path, the latter criterion is not strictly achieved when yarns layup in a contiguous manner. Thus the first approximation is that minor changes in cross-sectional area will be tolerated along the sweep path. Additionally, priority is given to experimentally determined dimensions. Unknown dimensions and geometry are determined from mesh-ability and geometric constraints. Randomness in the yarns and laminate are not considered in this study.

### *4.2.1. Yarn Orientations*

A simple algorithm is used to calculate the material orientation of an integration point bounded in an arbitrary yarn. Included in the mesh are the integration point locations, available using an in-house script. Each block is bounded by the three curves defining the yarn path. These can be defined analytically or piecewise using node sets and interpolation. Because the yarn orientation only varies by a rotation about the in-plane direction normal to the yarn symmetry, the problem is simplified into two dimensions. An optimization algorithm selects an angle of rotation defining a plane (line in 2D). The normal directions at the intersections of each bounding curve are obtained. Then a minimization is completed based on the weighted sum of the differences

between these normal angles and the input angle. The weight function is simply the inverse of the length of the line segment between the point of interest and the intersection point.

$$residual = \sqrt{\sum_{i=1}^{3}\left[w_i\left(\theta - \tan^{-1}\left(\frac{n_{xi}}{n_{yi}}\right)\right)\right]^2}$$

where $$w_i = \frac{|n_i|^{-1}}{\sqrt{|n_1|^{-2} + |n_2|^{-2} + |n_3|^{-2}}}$$

The material model utilizes the Initial Condition command which accesses the Exodus orientation data stored in the mesh to initialize internal state variables. An example is given in Figure 15 with the results shown in Figure 16.

The result is a piecewise angle distribution defined at each integration point. For fully integrated elements (8 integration points), orientation is uniquely defined at each point resulting in elements with multiple material orientations. Note that this in one method of many to assign material orientation to a woven yarn. For example, a weighted average of the curve tangents can be used at a given point location with acceptable results.

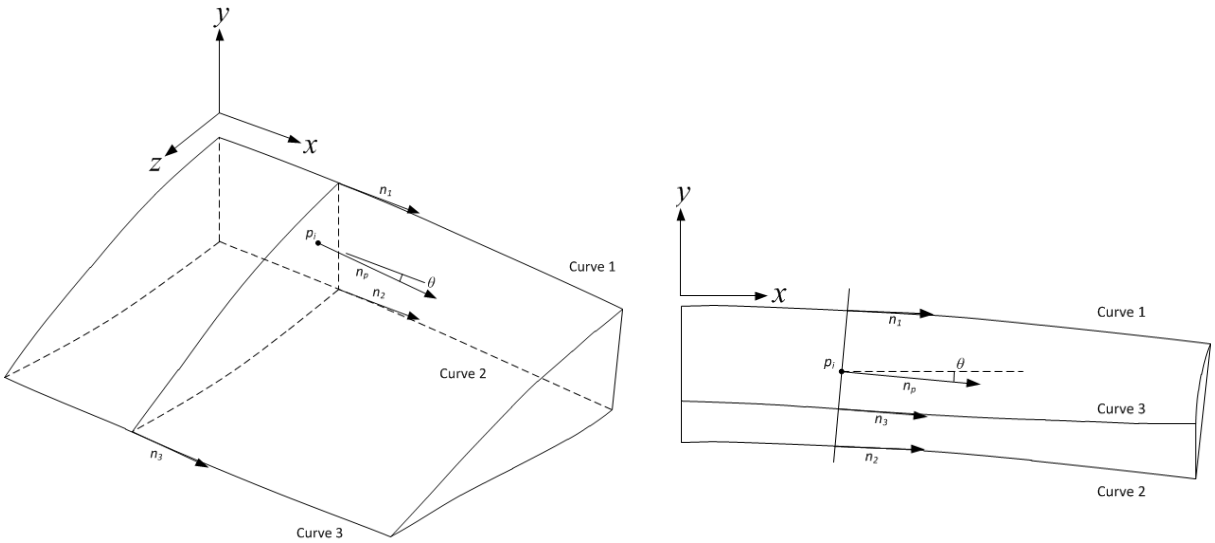


Figure 15. Illustration of the orientation optimization

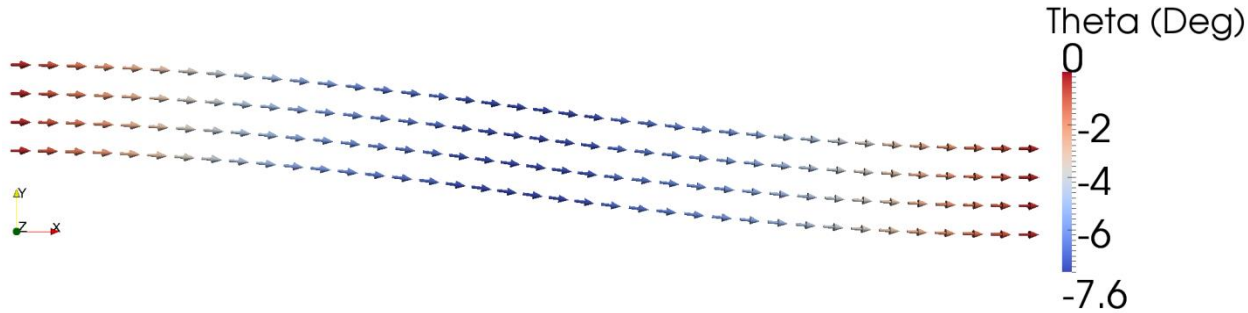


Figure 16. Output orientations for a yarn segment at symmetry plane written to each integration point

### *4.2.2. Plain Weave Geometries*

The following equations and methodology describe the geometry of a plain weave representative volume element [27]. The equations are mapped in three dimensions as vertices, the vertices are joined with curves through spline interpolation and curves bound surfaces that enclose individual volumes. The yarn section contains four unique volumes that can be reflected, rotated and translated to generate a single RVE.

The following dimensions describe the plain weave yarn geometry, see [27] for a complete description:

| | |
|---|---|
| $a_w$ | Warp peak to trough length |
| $a_f$ | Fill peak to trough length |
| $w_w$ | Warp yarn cross-sectional width |
| $w_f$ | Fill yarn cross-sectional width |
| $h_w$ | Warp yarn cross-sectional height |
| $h_f$ | Fill yarn cross-sectional height |
| $b_w$ | Warp sweep path amplitude |
| $b_f$ | Fill sweep path amplitude |

All dimensions are measured as if corners are sharp. Geometry modifications, such as fillets or chamfers, can be completed in the final stage. For this write-up, warp yarns and fill yarns are oriented in the *x* and *z* directions respectively. See Appendix A for a depiction of these curves.

#### 4.2.2.1. Inner Cross-Sections/Paths

"Inner" refers to a shared curve. The inner warp path corresponds to the inner fill cross-section and the inner fill path corresponds to the inner warp cross-section for the overlapping volumes. The inner fill cross-section/warp path curve is given as:

$$y(x) = \left(h_f - \frac{h_w}{2}\right)\cos\left(\frac{\pi x}{a_w}\right) - \frac{h_w}{2}$$

The inner warp cross-section/fill path curve is given as:

$$y(z) = \left(\frac{h_f}{2} - h_w\right)\cos\left(\frac{\pi z}{a_f}\right) + \frac{h_f}{2}$$

#### 4.2.2.2. Outer Paths

The outer paths in the overlap section are simply a normal projection from the inner paths where the thickness along the normal is *h*. In order to preserve continuity, the mid paths vary linearly between the outer paths and the adjacent cross-section.

#### 4.2.2.3. Outer Cross-Sections

The outer cross-sections at the yarn symmetry planes (peak or trough of the wave) are given as:

Warp yarn: $$y(z) = b_w \cos(\pi p_w z) - b_w + h_f$$

where

$$p_w = \frac{1}{w_w}\cos^{-1}\left(\left(\left(\frac{h_f}{2} - h_w\right)\cos\left(\frac{\pi w_w}{a_f}\right) - \frac{h_f}{2} + b_w\right)\Big/ w_f\right)$$

Fill yarn: $$y(x) = -b_f \cos(\pi p_f x) + b_f - h_w$$

where

$$p_f = \frac{1}{w_f}\cos^{-1}\left(\left(\left(\frac{h_w}{2} - h_f\right)\cos\left(\frac{\pi w_f}{a_w}\right) - \frac{h_w}{2} + b_f\right)\Big/ w_f\right)$$

#### 4.2.2.4. Warp and Fill Edges

Multiple techniques are available to generate a curve that ensures mesh continuity and qualitative accuracy. For this study, 5th order polynomials are chosen to represent the edges of the fill and warp yarns.

Warp yarn: $$y(x) = C_{1w}x^5 + C_{2w}x^4 + C_{3w}x^3 + C_{4w}x^2 + C_{5w}x + C_{6w}$$

Fill yarn: $$y(z) = C_{1f}z^5 + C_{2f}z^4 + C_{3f}z^3 + C_{4f}z^2 + C_{5f}z + C_{6f}$$

The coefficients of the above equations are solved using the following boundary conditions:

1. The start and end points of the curves must be located at the opposite cross-section's edge. (4 BCs)
2. Both curves intersect at point $(x, y, z) = (w_f, 0, w_w)$ and $(x, y, z) = (a_w - w_f, 0, a_f - w_w)$. (4 BCs)
3. The start and end points of the curves have zero slope. (4 BCs)

#### 4.2.2.5. Outer mid cross-sections

The inner warp and fill mid cross-sections for the four volume element are determined by the fill and warp edges as described in the previous section. The outer warp and fill mid cross-sections follow the constant mid thickness paths and are described by a similar formulation. A cross-section is generated by solving the periodic equations in the following form:

Warp cross: $$y(z) = C_{1w} \cos \frac{\pi z}{a_f} + C_{2w}$$

Fill cross: $$y(x) = C_{1f} \cos \frac{\pi x}{a_w} + C_{2f}$$

Boundary conditions of intersection at $(x, y, z) = (w_f, w_w, 0)$ and values corresponding to the constant thickness projection of warp and fill paths at $(x, y, z) = (w_f, 0, 0)$ and $(x, y, z) = (0, 0, w_w)$ respectively are applied. The resultant curve is mapped by interpolating from the intersection point to the projection point resulting in skewed mid cross-sections.

### *4.2.3. Satin Weave Geometries*

The individual curves that make up the undulated portion of the harness weave meso-structure are similar to those in the plain weave with a few exceptions. First, the yarns in the 0/90 region can overlap, resulting in the appearance of a uniform cross-section. Therefore, a fill yarn approaching the undulation must originate from an overlapping solid and must undercut the corresponding warp yarn at undulation and vice versa. This can explain the differences in warp and weft yarn counts for a balanced structure, where the cross-sectional areas of both yarns are equal. Second, for a first approximation, we generate a reduced RVE, with a single undulation and a proportional amount of non-undulating yarns compared to the complete RVE [17]. Figure 17 shows the 8HS RVE without matrix.

If zero overlap is assumed or determined from experiments, the balance of yarns can be ensured for a differing yarn count by adjusting the unknowns. Depending on the level of unknowns various parameters can be optimized. In a case where only the average lamina thickness is known, the warp to weft yarn thickness ratio is calculated based on the tow count. For a balanced composite this is translated as equal cross-sectional areas. Similarly, the cross-sectional shapes along the undulating yarn paths are adjusted to maintain equal areas. For elastic loading the two approaches provide similar results.

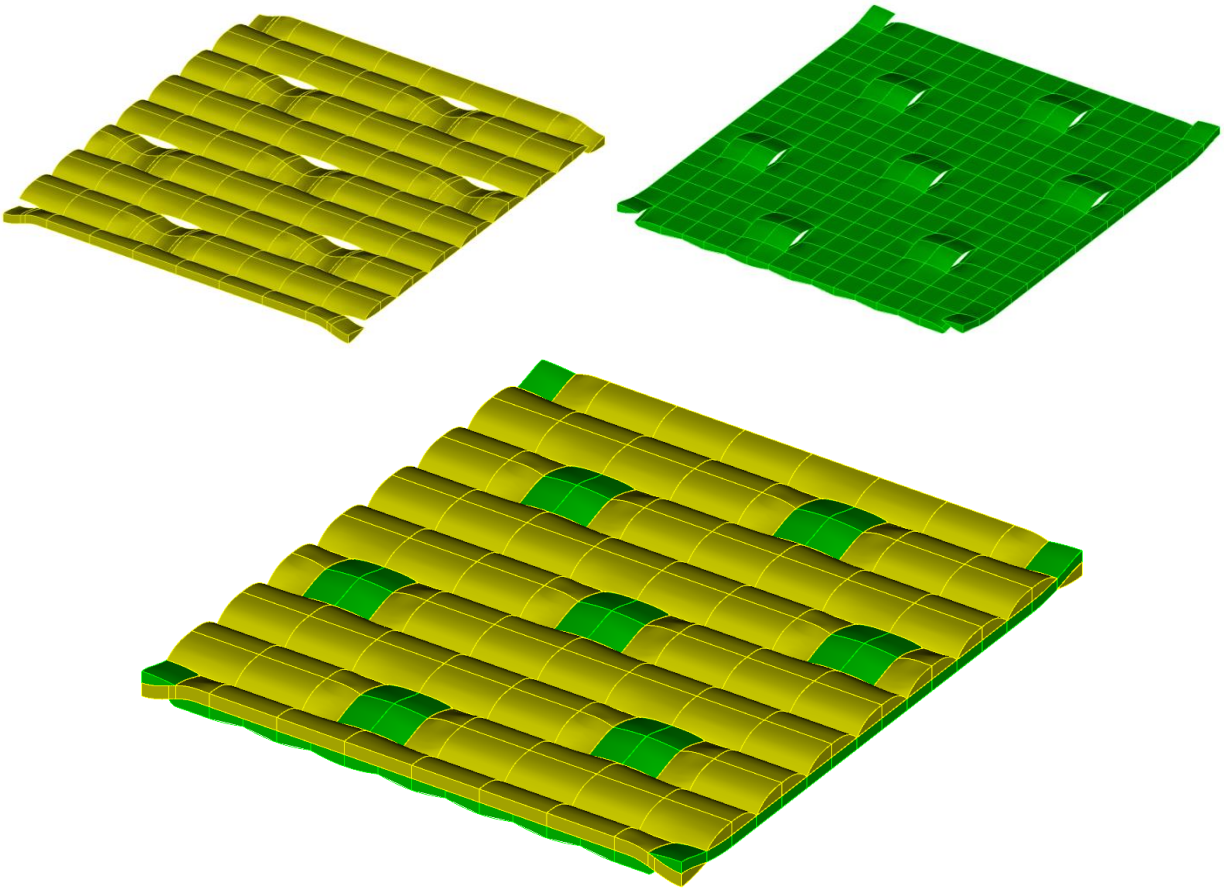

Figure 17. Yarns of an 8-harness satin weave

### *4.2.4. Voxelization of 8HS RVE*

The 8HS weave lamina unit cell is voxelized using a simple Python script that interacts with Cubit. Figure 18 show the voxel elements for the geometry shown in Figure 17. A voxel mesh is valuable because given a set of outer boundaries; the interior can be approximated without restrictions on complexity. For example an arbitrary laminate contains lamina that does not necessarily maintain planar contact, which has been assumed for other simulations in this study. Since a thorough investigation of the robustness of the voxel method is beyond the scope of this project, only issues such as elastic loading and mesh dependencies will be addressed. However, given the tools developed here and the broad implications of this method, a further study is recommended.

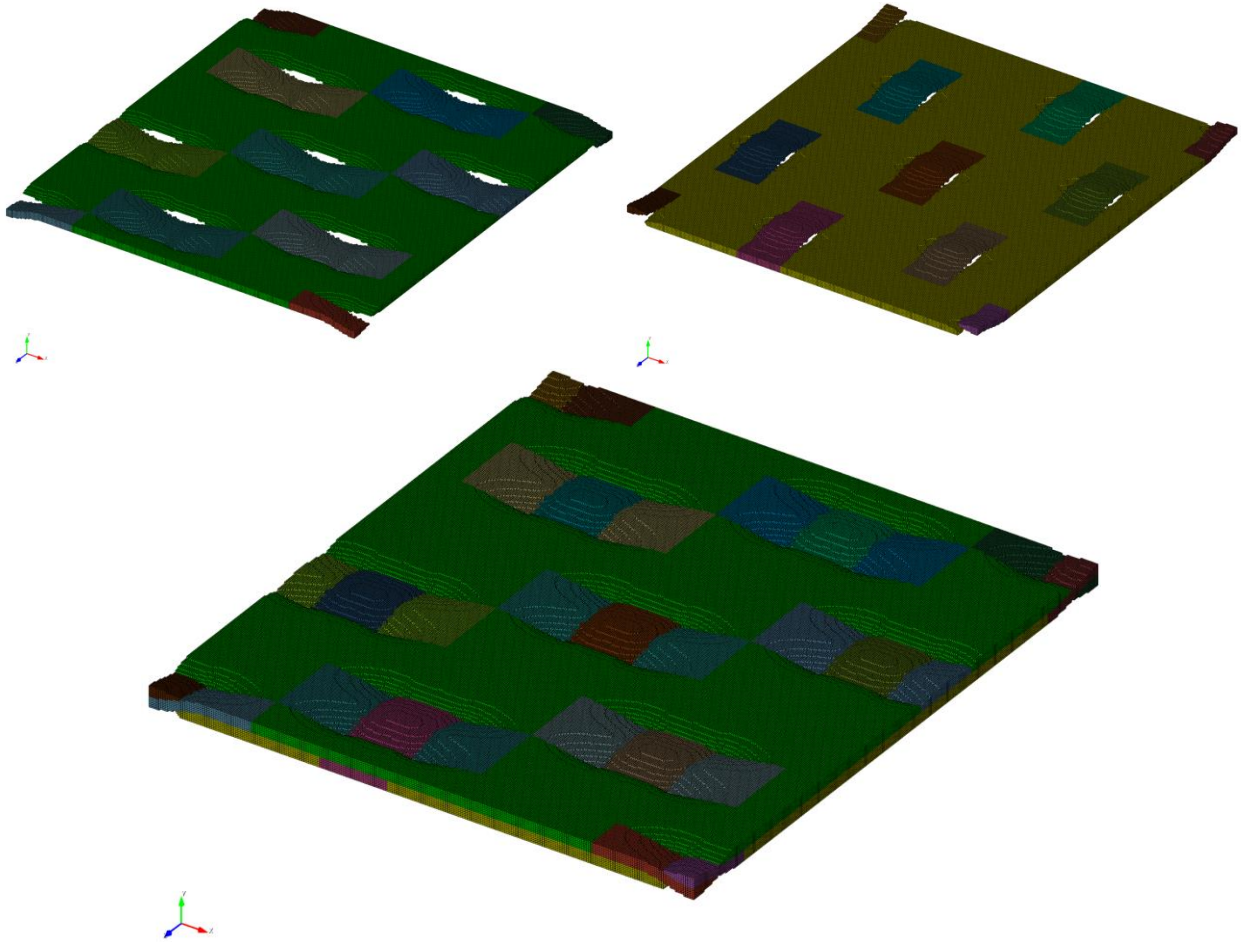

Figure 18.  Voxelized mesh of an 8-harness satin weave shown without matrix

# 5. BOUNDARY CONDITIONS AND MODEL IMPLEMENTATION

## 5.1. Boundary Conditions for RVEs

Two related boundary condition methodologies are investigated for this analysis: the RVE boundary conditions described by Wang et al. [28] and those automatically calculated with a RVE capability implemented in our in-house implicit solid mechanics code Sierra/Adagio. In general, the following describes the boundary condition formulation for both methods. First, the displacements on each parallel surface pair of the RVE rectangular prism as a function of Cartesian coordinates are given by

$$u_i(x_1, x_2, x_3) = \bar{\varepsilon}_{ik} x_k + u_i^*(x_1, x_2, x_3)$$

where $\bar{\varepsilon}_{ik}$ are the average strains in the RVE. The second term on the right hand side $u_i^*$ is a periodic function between RVEs ensuring continuity and is generally unknown. For linear elastic analysis, material constants can be determined by simply applying displacement fields and ensuring periodicity, which relies only on satisfying displacement differences on each pair of parallel faces. Thus, Wang et al. [28] shows that this equation reduces to

$$u_i^{j+} - u_i^{j-} = \bar{\varepsilon}_{ik}\left(x_k^{j+} - x_k^{j-}\right)$$

These boundary conditions are applied as periodic if $\bar{\varepsilon}_{ik} = 0$ or as displacements for the know (applied) quantities of $\bar{\varepsilon}_{ik}$. Boundary conditions applied in a damaging medium are more complicated however. The above described methodology allows for multiaxial stress states, then solves for the stiffness tensor directly. However, damage parameter estimation is typically done with uniaxial loading. Therefore, the above equation must be solved in order to ensure zero net traction in the unloaded directions. Since the in-house RVE method uses the strain rate ($\dot{\varepsilon}$), the above equation is written as

$$\dot{u}_i^{j+} - \dot{u}_i^{j-} = \dot{\varepsilon}_{ik}\left(x_k^{j+} - x_k^{j-}\right)$$

where $\dot{\varepsilon}_{ik}$ is the average strain rate over the RVE.

Methodology implemented in our in-house code simply applies the above boundary conditions in a multi-scale Finite Element Method. A reference element undergoing some prescribed kinematics passes the velocity gradient to the periodic RVE mesh that then returns volume average stresses. In a sense, the RVE serves as the constitutive equation for the reference model. The finite element method is used to apply appropriate BCs, ensuring convergence.

The strain rates are passed to the RVE model and applied as relative velocities to periodic surfaces. In the current implementation, the periodic boundary conditions require identical topology. Given an arbitrary RVE, this criterion is met using membrane elements and multi-point constraints.

If the RVE mesh is large, it may require multiple processors to run. Since Sierra models require all meshes to be decomposed on to each of the specified processes, both the reference mesh and the RVE mesh must contain at least as many elements as processors. Therefore, the reference region of a single element single RVE model must contain dummy elements. These elements can be given any material properties and boundary conditions and should remain detached from the element with the RVE material definition.

Cohesive surface elements are used to simulate intralaminar debonding between the yarns and matrix. At present, the RVE region does not allow for manually defined periodic surfaces, making coincident nodes incompatible. Shear loading and manual boundary conditions are provided to demonstrate this capability. An in-plane shear loading simulation of a plain weave RVE, shown in Figure 19, is provided as an example. Given the scope of this study, extensive use of this technology was not permitted. However, this capability serves as yet another vital advancement towards including all pertinent physics in the model.

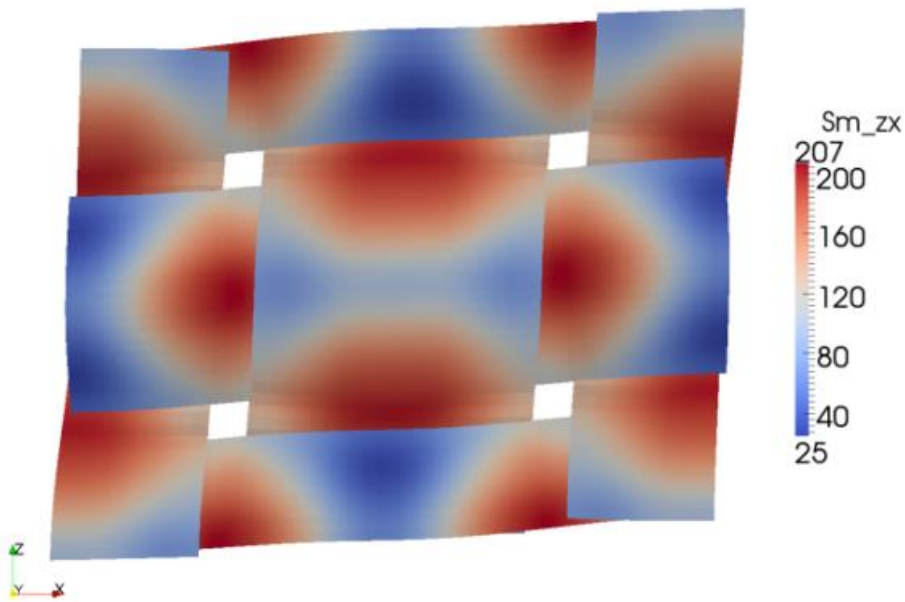


Figure 19. In-plane shear loading of a plain weave RVE with cohesive zone interface failure and material shear stress contours (matrix and cohesive elements not shown)

## 5.2. Verification

### *5.2.1. Boundary Conditions*

Two identical RVE meshes with elastic material parameters are implemented using both the periodic and RVE methodologies. First, Wang's six periodic boundary conditions are applied as follows. Six average strain tensors are applied to the faces of the RVE mesh. When $\bar{\varepsilon}_{ik} = 0$, the condition that $u_i^{j+} - u_i^{j-} = 0$ is ensured by periodic boundary conditions. The following provides the applied strain tensor and the output volume average stresses.

$$\bar{\varepsilon}_{ik} = \begin{bmatrix} 0.00151 & 0 & 0 \\ 0 & 0 & 0 \\ 0 & 0 & 0 \end{bmatrix}; \qquad \bar{\sigma}_{ik} = \begin{bmatrix} 90.93 & 0 & 0 \\ 0 & 7.014 & 0 \\ 0 & 0 & 15.50 \end{bmatrix} \text{(MPa)}$$

$$\bar{\varepsilon}_{ik} = \begin{bmatrix} 0 & 0 & 0 \\ 0 & 0.00195 & 0 \\ 0 & 0 & 0 \end{bmatrix}; \qquad \bar{\sigma}_{ik} = \begin{bmatrix} 20.13 & 0 & 0 \\ 0 & 108.8 & 0 \\ 0 & 0 & 9.202 \end{bmatrix} \text{(MPa)}$$

$$\bar{\varepsilon}_{ik} = \begin{bmatrix} 0 & 0 & 0 \\ 0 & 0 & 0 \\ 0 & 0 & 0.00311 \end{bmatrix}; \qquad \bar{\sigma}_{ik} = \begin{bmatrix} 14.40 & 0 & 0 \\ 0 & 14.92 & 0 \\ 0 & 0 & 30.02 \end{bmatrix} \text{(MPa)}$$

$$\bar{\varepsilon}_{ik} = \begin{bmatrix} 0 & 0.005 & 0 \\ 0.005 & 0 & 0 \\ 0 & 0 & 0 \end{bmatrix}; \qquad \bar{\sigma}_{ik} = \begin{bmatrix} 0 & 42.48 & 0 \\ 42.48 & 0 & 0 \\ 0 & 0 & 0 \end{bmatrix} \text{(MPa)}$$

$$\bar{\varepsilon}_{ik} = \begin{bmatrix} 0 & 0 & 0.005 \\ 0 & 0 & 0 \\ 0.005 & 0 & 0 \end{bmatrix}; \qquad \bar{\sigma}_{ik} = \begin{bmatrix} 0 & 0 & 25.78 \\ 0 & 0 & 0 \\ 25.78 & 0 & 0 \end{bmatrix} \text{(MPa)}$$

$$\bar{\varepsilon}_{ik} = \begin{bmatrix} 0 & 0 & 0 \\ 0 & 0 & 0.005 \\ 0 & 0.005 & 0 \end{bmatrix}; \qquad \bar{\sigma}_{ik} = \begin{bmatrix} 0 & 0 & 0 \\ 0 & 0 & 26.11 \\ 0 & 26.11 & 0 \end{bmatrix} \text{(MPa)}$$

These loads are implemented sequentially. The homogenized stress strain relationship of the elastic system can be defined as

$$\bar{\sigma}_{ij} = \boldsymbol{C}_{ijkl}\bar{\varepsilon}_{kl}$$

Solving each term from the populated data directly, the following stiffness tensor is given in contracted form

$$[\boldsymbol{C}] = \begin{bmatrix} 60.2 & 10.3 & 4.63 & 0 & 0 & 0 \\ 10.3 & 55.8 & 4.80 & 0 & 0 & 0 \\ 4.65 & 4.72 & 9.65 & 0 & 0 & 0 \\ 0 & 0 & 0 & 8.50 & 0 & 0 \\ 0 & 0 & 0 & 0 & 5.16 & 0 \\ 0 & 0 & 0 & 0 & 0 & 5.22 \end{bmatrix} \text{(GPa)}$$

For simplicity only the symmetric part is used.

$$\overline{\boldsymbol{C}}_{ijkl} = \frac{1}{2}\left(\boldsymbol{C}_{ijkl} + \boldsymbol{C}^{T}_{ijkl}\right)$$

The compliance tensor is then

$$[\bar{\boldsymbol{S}}] = [\bar{\boldsymbol{C}}]^{-\mathbf{1}} = \begin{bmatrix} \frac{1}{E_{11}} & \frac{-\nu_{21}}{E_{22}} & \frac{-\nu_{31}}{E_{33}} & 0 & 0 & 0 \\ \frac{-\nu_{12}}{E_{11}} & \frac{1}{E_{22}} & \frac{-\nu_{32}}{E_{33}} & 0 & 0 & 0 \\ \frac{-\nu_{13}}{E_{11}} & \frac{-\nu_{23}}{E_{22}} & \frac{1}{E_{33}} & 0 & 0 & 0 \\ 0 & 0 & 0 & \frac{1}{2G_{12}} & 0 & 0 \\ 0 & 0 & 0 & 0 & \frac{1}{2G_{13}} & 0 \\ 0 & 0 & 0 & 0 & 0 & \frac{1}{2G_{23}} \end{bmatrix}$$

The orthotropic homogenized elastic constants are easily solved.

$$E_{11} = 56.8 \text{ GPa}$$
$$E_{22} = 52.4 \text{ GPa}$$
$$E_{33} = 9.00 \text{ GPa}$$
$$G_{12} = 4.25 \text{ GPa}$$
$$G_{13} = 2.58 \text{ GPa}$$
$$G_{23} = 2.61 \text{ GPa}$$
$$\nu_{12} = 0.150$$
$$\nu_{13} = 0.407$$
$$\nu_{23} = 0.427$$

Applying the RVE region to the same geometry, the elastic parameters are solved directly from the stresses and strains in the reference model. For uniaxial loading in the 11 direction for example,

$$E_{11} = \frac{\bar{\sigma}_{11}}{\bar{\varepsilon}_{11}}$$

$$\nu_{12} = -\frac{\bar{\varepsilon}_{22}}{\bar{\varepsilon}_{11}}$$

$$\nu_{13} = -\frac{\bar{\varepsilon}_{33}}{\bar{\varepsilon}_{11}}$$

The remaining parameters are found and a symmetric stiffness tensor is formulated. The resulting homogenized elastic constants are

$$E_{11} = 56.8 \text{ GPa}$$
$$E_{22} = 51.9 \text{ GPa}$$
$$E_{33} = 8.98 \text{ GPa}$$

$$G_{12} = 4.25 \text{ GPa}$$
$$G_{13} = 2.49 \text{ GPa}$$
$$G_{23} = 2.51 \text{ GPa}$$
$$\nu_{12} = 0.152$$
$$\nu_{13} = 0.411$$
$$\nu_{23} = 0.424$$

The in-plane elastic results from both methods compare well. For elastic properties, Wang's method is preferable due to the extremely high computational time required for multi-scale modeling. Thus, the RVE region will primarily be implemented for damage property estimation.

### *5.2.2. Micro RVE Mesh Convergence*

A mesh convergence study is undertaken for a single sampling of fibers. The stress-strain curves and related peak stress measurements are shown in Figures 20 and 21 respectively. The ratios on the abscissa should be read as one over the minimum number of elements between fibers. The models show excellent mesh convergence/insensitivity for the elastic modulus. However, the rate of convergence for the peak stress is very low. Nevertheless, the medium mesh density with a minimum of two elements between fibers produces results with identical crack paths and similar strength values compared to the finer versions. Therefore, for this study the medium mesh is used to estimate unidirectional material properties.

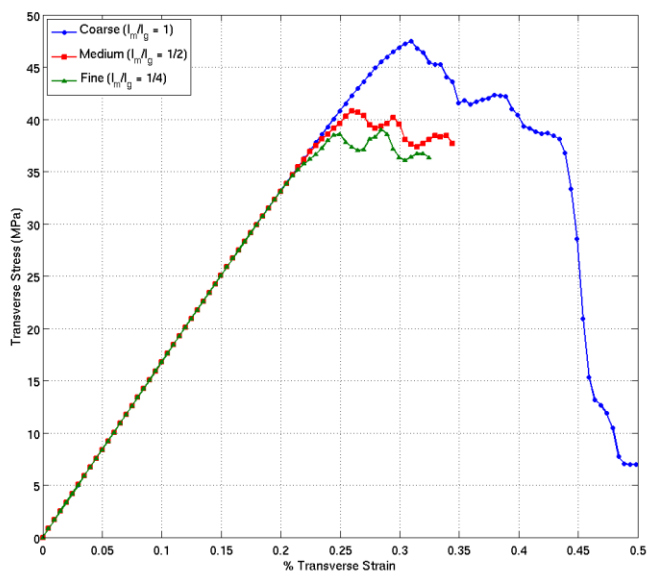


Figure 20. Homogenized tensile response for single coarse sample with different mesh sizes

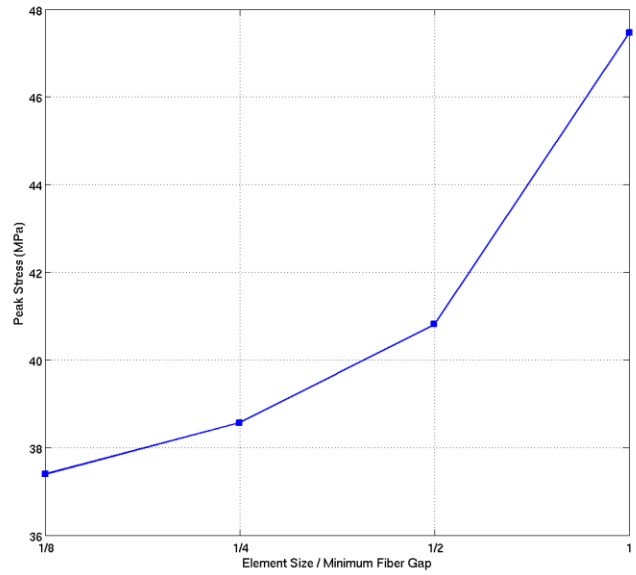


Figure 21. Mesh convergence of uniaxial transverse peak load for random fiber composites

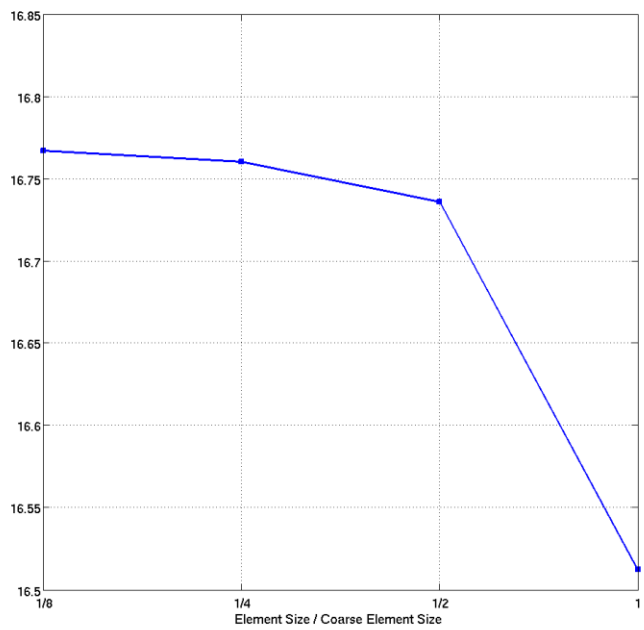


Figure 22. Transverse modulus verse mesh size ratio for a random glass fiber model

### *5.2.3. Meso RVE Mesh Convergence*

The meso-scale RVE simulations suffered from poor convergence in the implicit solid-mechanics code Sierra. This is magnified with finer meshes. Nevertheless, mesh convergence studies are completed on the 8HS GFRP overlapping reduced meso-geometry for elastic properties and a plain weave RVE for shear cracking. Shear loading of the plain weave RVE is

done up to 2.16 % strain. This value ensures small strains and convergence in the fine mesh implicit run.

The poorest convergence in the elastic runs is shown for shear loading. The in-plane shear moduli for three mesh sizes in the 8HS meso geometry are shown in Table 1. The values are shown to be insensitive to mesh size within the range tested.

Figure 23 shows the volume average in-plane shear stress values for plain-weave RVE. The material properties for both the elastic to failure and plasticity models are adjusted for mesh size. While the mesh shows convergence, the rate is low.

Table 1. In-plane shear moduli 8HS GFRP

| **Mesh Size ($\mu m$)** | **$G_{12}$ (GPa)** |
|---|---|
| 100 | 3.827 |
| 50 | 3.828 |
| 25 | 3.826 |
| 12.5 | 3.824 |

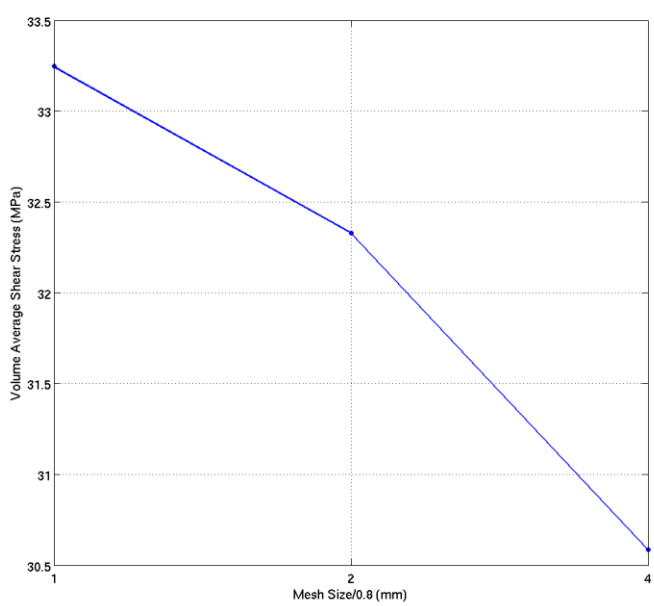


Figure 23. Mesh convergence of the volume average shear stress at $\gamma_{12}$ = 2.16 % for a plain weave geometry

When possible the mean-quadrature hexahedral element is implemented. In some cases, tetrahedral elements are used to ease meshing. The tetrahedral elements produced similar results

to hexahedral under elastic loading, but are questionable with damage and failure. Tetrahedral elements are used only in elastic analysis of the overlapping satin weave mesh.

### *5.2.4. Voxel Mesh Convergence*

The first mesh convergence studies are conducted for the geometry described in section 4.2.4. Voxel meshes are not suited for stress concentration analysis. However, the homogenized stress strain relationship may be convergent or insensitive to mesh refinement. Therefore, estimating elastic properties with a voxel mesh should be convergent or insensitive. First, a mesh dependent solution is illustrated by simulating a single (not reduced) RVE for thermal stress concentration analysis given orthotropic coefficients of thermal expansion (CTE) in the yarns. An unconstrained RVE is used to find flexure and peak residual stress respectively. The non-convergent results are as follows:

Table 2. Max out-of-plane displacement of a GFRP 8HS for $\Delta T = 50$ C

| **Mesh Size ($\mu m$)** | **Max out-of-plane displacement ($\mu m$)** |
|---|---|
| 100 | 69.74 |
| 50 | 68.75 |
| 25 | 67.91 |

Table 3. Max stress of a unloaded GFRP 8HS for $\Delta T = 50$ C

| **Mesh Size ($\mu m$)** | **Peak Stress (MPa)** |
|---|---|
| 100 | 106.7 |
| 50 | 122.5 |
| 25 | 156.1 |

While stress concentrations in a voxel mesh will likely prevent mesh convergence with computational reasonable mesh densities for peak stresses, the homogenized elastic properties may be convergent or insensitive to mesh. Figure 24 shows the absolute difference of all the orthotropic elastic properties from the finest mesh implemented. While the trend is not convergent in this region, the values do show moderate insensitivity. Therefore, this method along with boundary conditions discussed earlier may be valuable for arbitrary meso/micro structures.

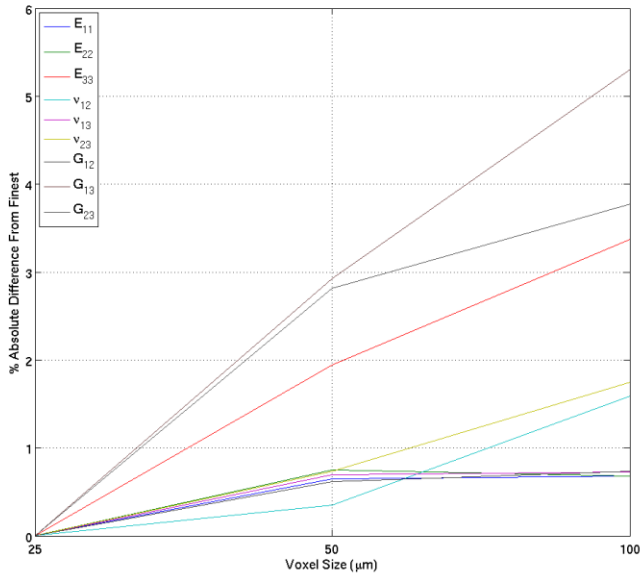


Figure 24. 8HS GFRP elastic properties voxel mesh convergence plot

### *5.2.5. Elements*

Tetrahedral elements produced similar results to hexahedral under elastic loading. Similarly, tetrahedral elements matched well at the initiation of cracking. However, these elements did not consistently converge to a solution and while meshing is trivial, a solution was rarely guaranteed. The overlapping satin weave mesh uses tetrahedral elements. The mesh can be generated using hexahedral elements, but automation was not achieved. Other elements, such as nodal based tetrahedral, 10 node tetrahedral and fully integrated hexahedral, where tested. For this report only tetrahedral elements for elastic analysis and mean-quadrature for elastic and damage analysis are presented.

# 6. RESULTS AND DISCUSSION

Responses not easily obtained using experimental methods are of primary interest. These include biaxial tension, compression, in and out-of-plane shear, residual stress distributions in curing, damage and plastic initiation and evolution, and off axis coupling effects. In the presence of limited data, simple experiments are used in addition to constituent properties to calibrate the meso-mechanical response.

## 6.1. Elastic Properties

### *6.1.1. Plain-Weave Graphite-Epoxy*

The macroscopic plain weave response is modeled and mechanically averaged for one set of statistical responses and compared to the plain-weave graphite-epoxy data presented in [27]. The results are shown in Table 4 with data from a similar modeling study found in [29]. The easily measured in-plane yarn dimensions are sampled while the thicknesses and yarn shapes are determined by the balance of cross-sectional areas. This approach assumes constant fiber volume fraction in the yarn based on nominal dimensions and an iso-phase layup.

Table 4. Carbon-epoxy plain weave elastic properties

| Property | Ito and Chou [27] (Std. Dev.) | Barbero [29] | Simulated |
|---|---|---|---|
| $E_{11}$ | 43.5 (2.12) | 44.6 | 45.0 |
| $E_{22}$ | N/A | 43.7 | 41.6 |
| $E_{33}$ | N/A | 10.0 | 7.70 |
| $\nu_{12}$ | N/A | 0.062 | 0.141 |
| $\nu_{13}$ | N/A | 0.404 | 0.432 |
| $\nu_{23}$ | N/A | 0.411 | 0.445 |
| $G_{12}$ | N/A | 3.61 | 2.97 |
| $G_{13}$ | N/A | 2.90 | 2.30 |
| $G_{23}$ | N/A | 2.91 | 2.33 |

A Latin Hypercube Sampling (LHS) of the characteristic parameters is used for model generation. Then a single layer structured mesh is used for macroscopic mechanical averaging, where each element is assigned one homogenized set of parameters from a single meso-scale representative volume. The warp elastic modulus ($E_{11}$) is given for one sampling of geometric parameters as 45.0 GPa, which matches well with the experimental responses. The individual

homogenized RVE elastic moduli have a mean of 45.1 and a standard deviation of 3.88. The distribution of 100 samplings is shown in Figure 25.

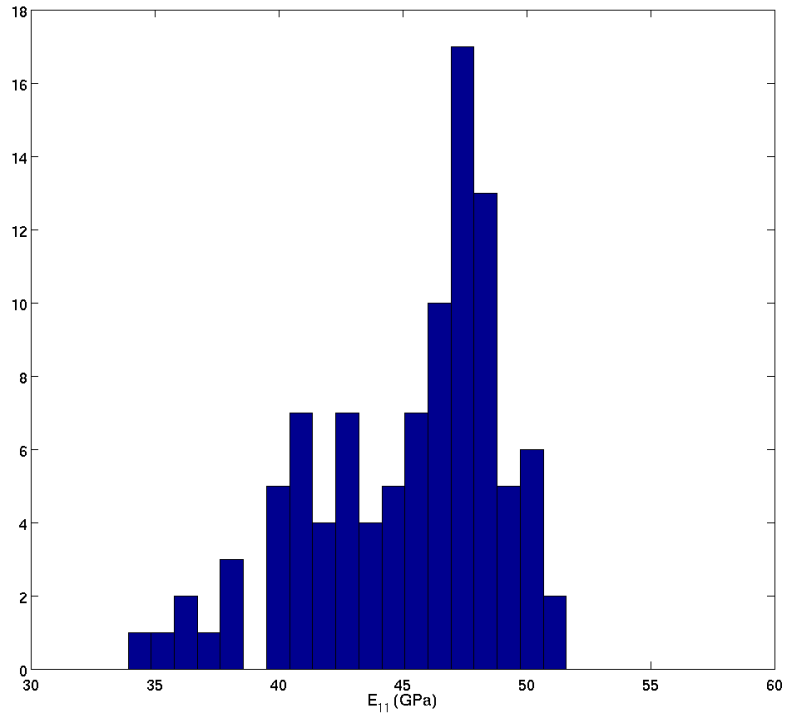


Figure 25. Distribution of the axial modulus

In general, a distribution of in-plane elastic responses is best obtained through experiments. However, the methodology presented here provides out-of-plane properties and insight into stress concentration for damage initiation and failure analysis.

### *6.1.2. 8HS Glass-Epoxy*

The homogenized elastic response of the 8 harness satin weave E-glass reduced unit cell predicts a range of warp modulus between 23.4 - 26.4 GPa for the manufacturer's low and high fiber volume fractions respectively. This matches well with the experiments, where $E_{11}$ = 24.82 GPa with a standard deviation of 0.56 GPa. The two sets of elastic parameters are shown in Table 5.

Table 5. E-glass 8HS elastic properties

| Property | Measured (Std. Dev.) | Simulated |
|---|---|---|
| $E_{11}$ | 24.8 (0.56) | 23.4 - 26.4 |
| $E_{22}$ | 23.1 (0.39) | 21.1 - 25.0 |
| $E_{33}$ | N/A | 8.78 - 10.4 |
| $\nu_{12}$ | 0.13 (0.01) | 0.117 - 0.124 |
| $\nu_{13}$ | N/A | 0.371 - 0.345 |
| $\nu_{23}$ | N/A | 0.376 - 0.349 |
| $G_{12}$ | 3.45 | 3.40 - 4.47 |
| $G_{13}$ | N/A | 2.67 - 3.13 |
| $G_{23}$ | N/A | 2.61 - 3.04 |

### *6.1.3. 8HS Carbon-Epoxy*

Similar simulations are completed for 8-harness carbon-epoxy. Carbon fibers are highly anisotropic; therefore, the transverse micro-scale elastic properties are calibrated (inverse micromechanics) from manufacturers specification [30]. The transverse modulus of a single AS4 carbon fiber is calculated as 14.2 GPa and transverse shear modulus of 13.7 GPa. The micro-scale elastic parameters of a UF3362 polymer resin reinforced with 77% - 87% AS4 3K carbon fibers are shown in Table 6. This is the fiber volume fraction in a yarn given 71.3 % yarns and 55% - 62% total fiber volume fraction (see Figure 10).

Table 6. Unidirectional CFRP (yarn) properties

| Property | $V_f = 0.77$ | $V_f = 0.87$ |
|---|---|---|
| $E_{11}$ | 178.6 | 201.4 |
| $E_{22}$ | 9.59 | 11.4 |
| $\nu_{12}$ | 0.302 | 0.296 |
| $\nu_{23}$ | 0.366 | 0.336 |
| $G_{12}$ | 3.54 | 4.32 |
| $G_{23}$ | 3.49 | 4.23 |

Table 7. 8HS CFRP elastic properties

| Property | Measured (*Estimated) | Simulated |
|---|---|---|
| $E_{11}$ | 61.0 – 73.0 | 68.1 – 76.9 |
| $E_{22}$ | 55.0* | 65.5 – 74.0 |
| $E_{33}$ | 9.78* | 8.19 – 8.98 |
| $\nu_{12}$ | 0.048 | 0.0460 – 0.0464 |
| $\nu_{13}$ | 0.30* | 0.416 – 0.399 |
| $\nu_{23}$ | 0.30* | 0.417 – 0.399 |
| $G_{12}$ | 3.71 – 4.60* | 4.15 – 5.89 |
| $G_{13}$ | 4.60* | 3.00 – 3.53 |
| $G_{23}$ | 4.60* | 2.99 – 3.51 |

## 6.2. Tensile loading of 8HS GFRP

Transverse cracking of the weft yarns under warp direction tensile loading is marked by a knee in the stress-strain relationship (see Section 3.4). Micromechanical simulations are used to estimate the distribution of transverse failure strengths in the yarns based on geometrical variations. Matrix plasticity and failure are based on $J_2$ and maximum equivalent plastic strain criterion. The resulting random distribution of strengths are used to calibrate a continuum damage constitutive model based on the crack band theory [1, 2, 12]. The random and structured meso-mechanical simulations produce peak uniaxial transverse stresses between 41 – 71 MPa for GFRP and fracture energy of 0.050 MPa-mm [22]. An example of the elastic properties for a fiber volume fraction of 68% estimated by a random fiber simulation is given in Table 8. Figure 26 gives an example of the finite element representation of the transverse cracking. Similarly, Figure 27 shows the generation of these cracks in experiments. Qualitatively similar results are shown in [31].

Table 8. Unidirectional GFRP (yarn) elastic properties

| Property | Value |
|---|---|
| $E_{11}$ | 51.6 GPa |
| $E_{22}$ | 15.3 GPa |
| $\nu_{12}$ | 0.238 |
| $\nu_{23}$ | 0.361 |
| $G_{12}$ | 5.58 GPa |
| $G_{23}$ | 5.63 GPa |

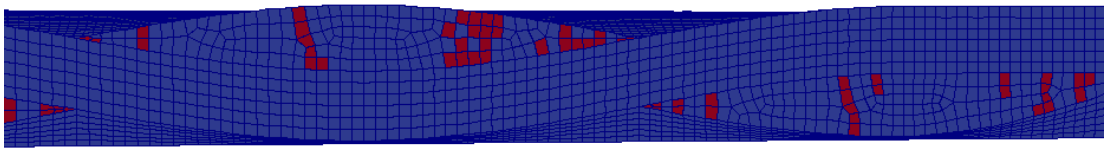

Figure 26. Transverse (fill) yarn cracks shown as failed elements in red

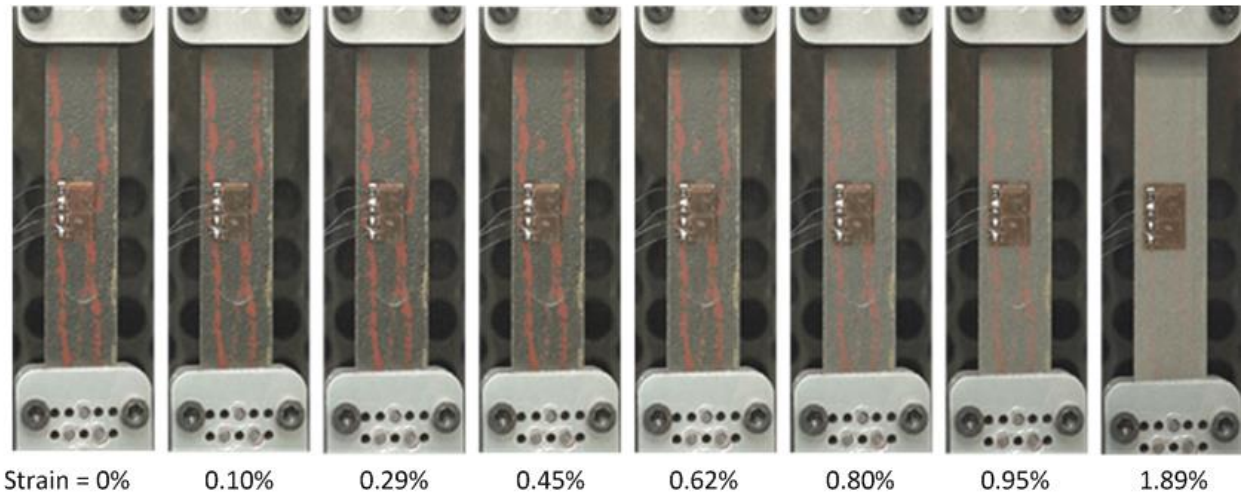


Figure 27. Crack cloud experimental example for GFRP under uniaxial tension

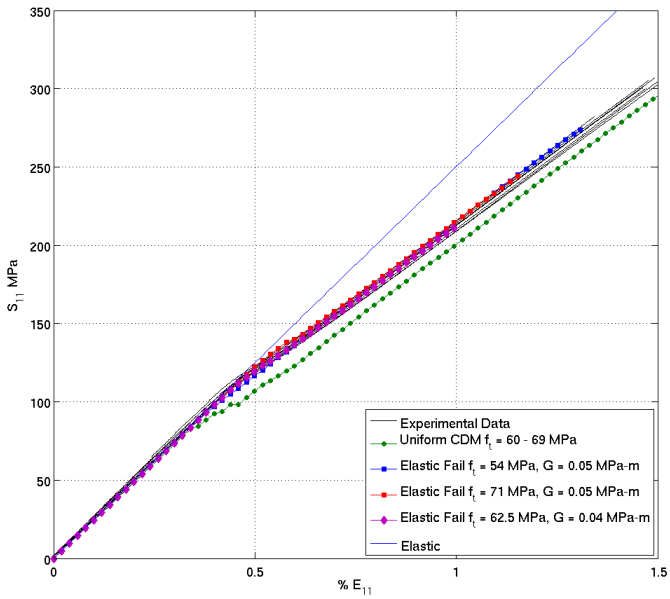


Figure 28. Stress versus strain for axial (warp) tension in GFRP 8HS

Figure 28 provides a sampling of the homogenized mesomechanical stress strain responses and the experimental data. A linear elastic stress strain curve is shown in order to provide reference

to the loss of stiffness due to transverse cracking. Four results from zero gap non-overlapping meso hexahedral mesh with RVE solved boundary conditions are given.

1) Softening prediction from a uniform distribution of failure mechanisms on the effective stress based on hexagonal packed micromechanical estimates and CDM damage evolution. The failure stresses are distributed uniformly from 60 to 69 MPa, based on a normal distribution of volume fractions with hexagonal packing. Figure 29 shows the approximate uniform distribution. The stress-strain relationship assumes damage is the cumulative probability of the failure distribution function from unloaded to a given stress. The damage evolution parameters are found using an optimization script. Therefore, for a transverse uniaxial load up to an effective stress of 69 MPa, the actual stress has decayed to zero. It should be noted, however, that given an energy equivalence CDM formulation the actual strain goes to infinity as stress goes to zero.
2) The maximum randomly distributed micromechanical estimate of peak stress with elastic to failure and crack band theory. The minimum and maximum peak uniaxial stresses are $f_T$ = 41 and 54 MPa respectively. A failure stress of 41 MPa is not included, because it under predicts crack initiation.
3) Hexagonal packed micromechanical estimate of peak stress of $f_T$ = 71 MPa with elastic to failure and crack band theory.
4) Finally, it should be reiterated that the GFRP results are derived from micromechanical simulations with constituent properties and the geometry is taken from direct measurements. However, based on the insight gained from previous simulations, a "best guess" curve is given ($f_T$ = 62.5 MPa, $G$ = 0.040 MPa-mm).

Both damage/failure methods predict elastic stiffness, crack initiation point and post cracking tangent stiffness fairly well. The elastic to failure method incorporating crack band theory and control failure better predicts the gradual crack growth over a strain range. CDM predations under represent the energy dissipation resulting in an artificially small fracture toughness and sudden crack growth. When using an implicit solver for strain localization, a control failure algorithm is necessary in order to prevent failure clouds, or large areas of failed elements without localization. In future cases, all softening material models will include an orthotropic crack-flag technique.

Similar results are obtained when implementing the plain weave geometries given in [27]. Statistical distributions of geometries and constituent properties are easily included to obtain a range of meso-structural responses.

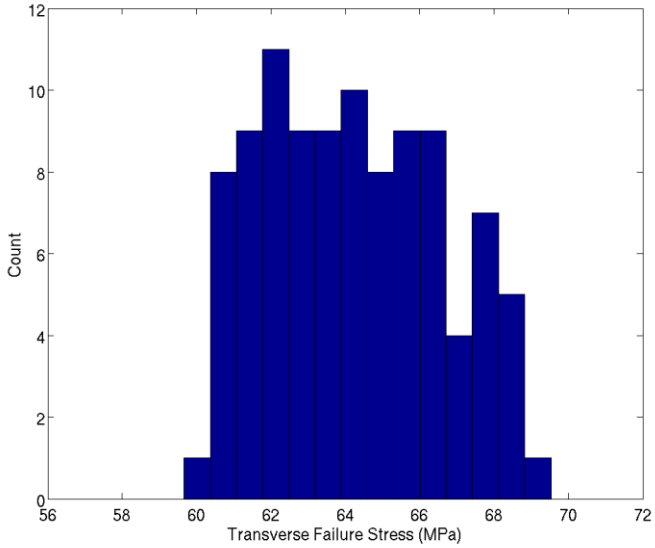


Figure 29. Approximate uniformly distributed transverse strengths for unidirectional GFRP

## 6.3. Shear loading of 8HS GFRP

The yarns in the reduced 8HS GFRP RVE are assigned the orthotropic elastic to fail material. Given the known mode I and mode II interlaminar fracture toughnesses, the yarn toughness values will assume the same ratio. Therefore, the yarn material is modeled with an upper limit peak stress calculated from micromechanics of 40 MPa and a toughness $G_{II}$ = 0.16 MPa-mm. The simulation is done with a RVE region with an orientation associated with the +45° axis. This means that tensile loading of the reference region applies a 45° transformed strain-rate to the RVE region. Figure 30 shows the experimental net stress versus axial strain results with volume average tensile stress versus strain for the 45° RVE simulation.

The strain in the experimental data is slightly offset to better represent linear elasticity. While, the elastic response matches well, the micromechanical analyses seem to under predict the shear strength. Calibration is not necessary for this simulation, because better results are expected with an interactive failure criterion with plasticity and damage prior to failure and cohesive zone elements.

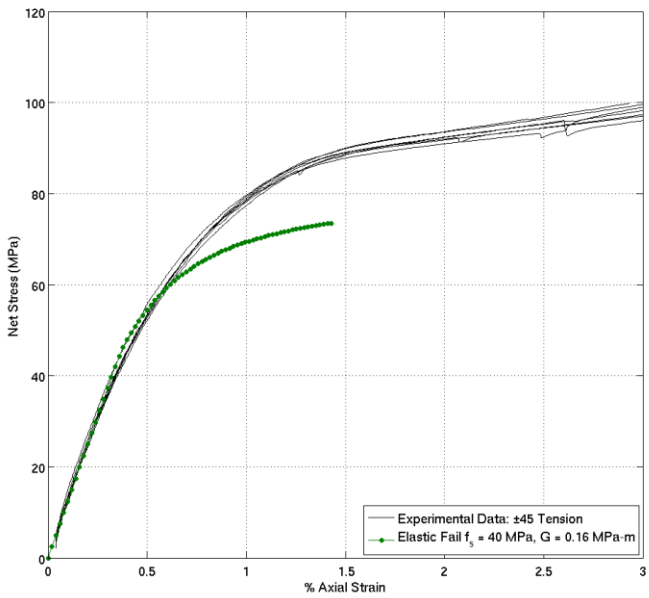


Figure 30. Stress versus strain for the in-plane shear of GFRP 8HS

## 6.4. Damage/Plastic Properties from Shear

Figures 31 and 32 show the load controlled cyclic in-plane shear response of a plain weave RVE. Plastic strains and damage evolution can be obtained from this homogenized response.

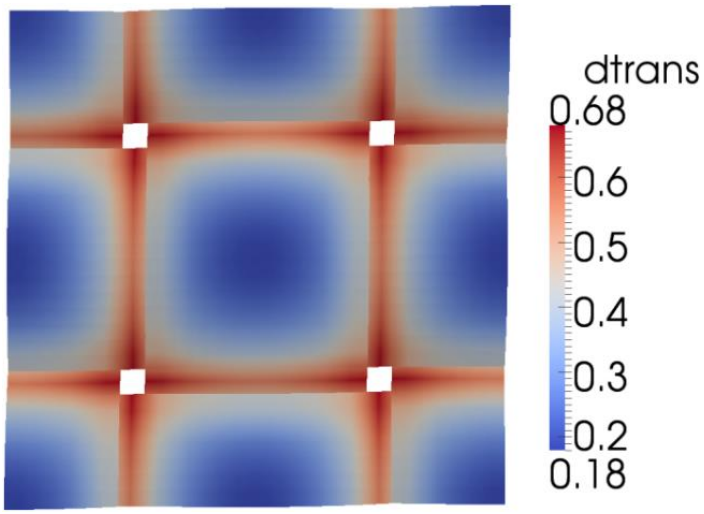


Figure 31. Transverse damage distribution of a plain weave RVE under pure in-plane shear (shown without matrix)

For continuum damage evolution of the macroscopic homogenized material [1, 2]; coefficients describing Hill plasticity [11], crack closure and damage evolution are easily obtained using a series of RVE simulations. Similar to the methodology presented in [1], the data is reduced to elastic damage and plastic strain evolution shown in Figures 33 and 34 respectively. The

calibrated coupled orthotropic elastic-plastic damage material model response is shown in Figure 32. A statistical distribution of the parameters characterizing the variability of the responses can also be obtained.

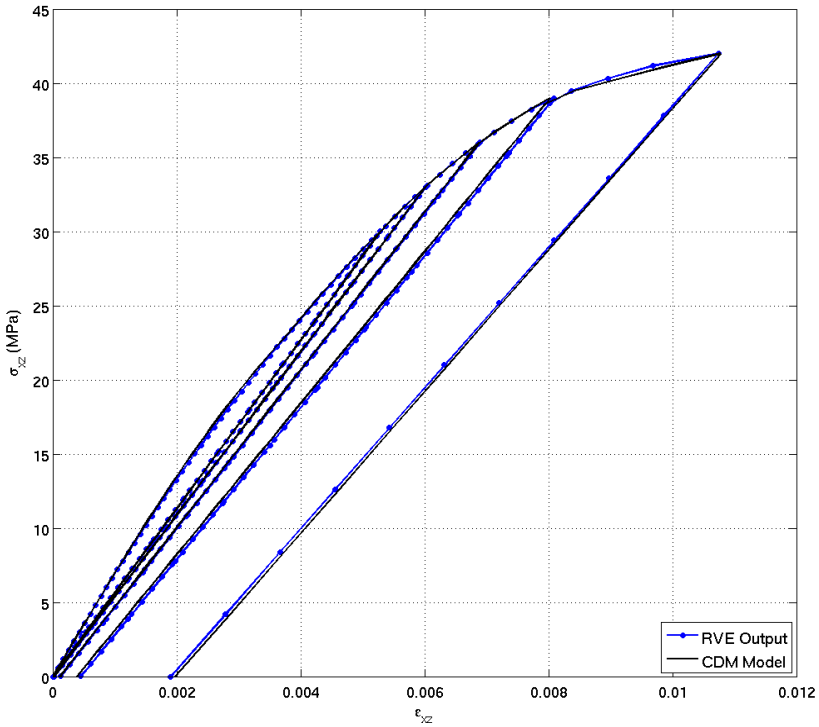


Figure 32. Cyclic shear response of a plain weave RVE

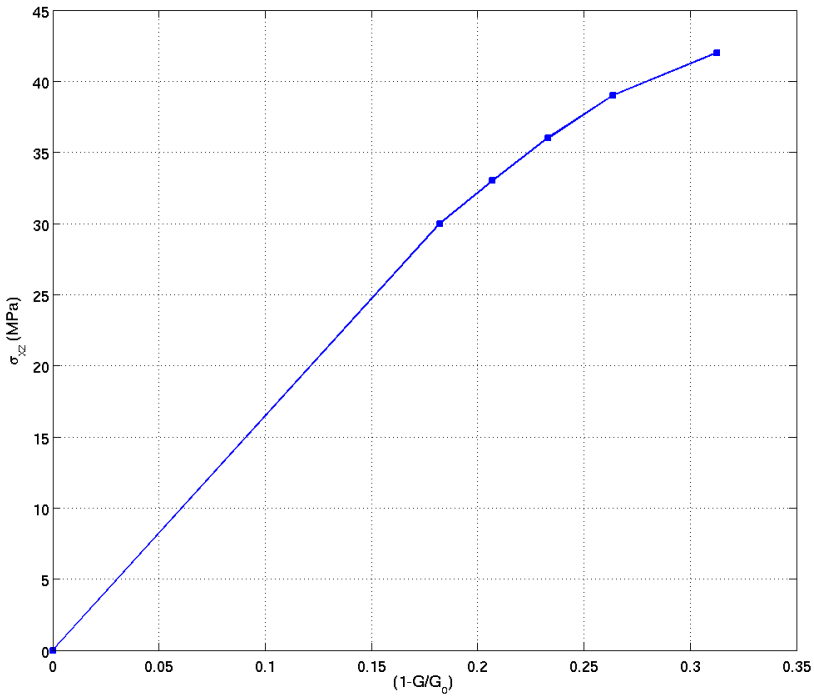


Figure 33. Damage accumulation under shear

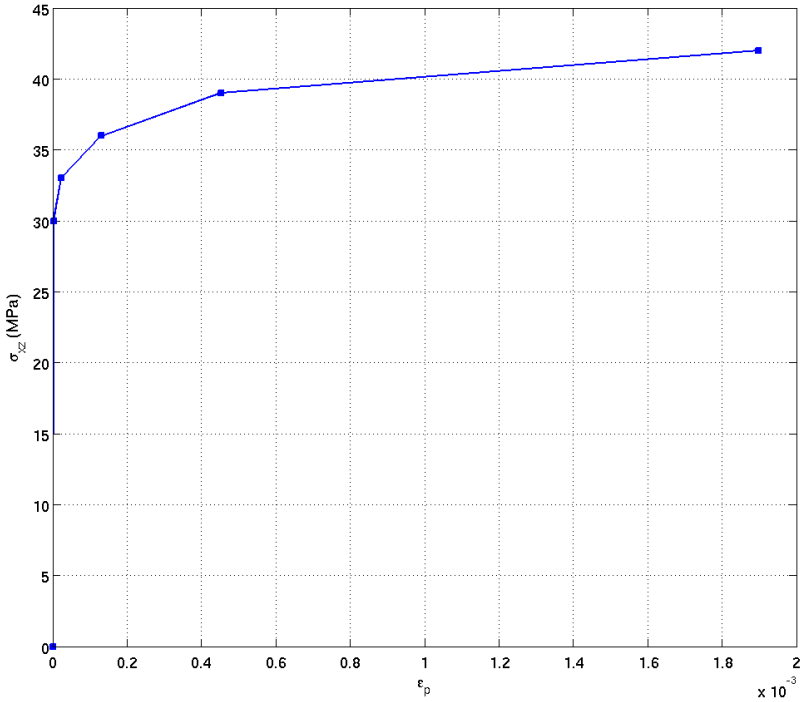


Figure 34. Plastic strain accumulation under shear

## 6.5. Archives and Products

The following list is meant to aid a potential user in accessing material models and scripts. While all tools are available for use, only a select few are refined enough for general access. For the material models, many exist only on a local version of the Sierra software because release of these models requires additional verification and documentation. Additionally, while every effort is taken to produce user-friendly scripts for post and pre-processing and mesh generation, most require a unique skillset and user support. The following is a list of available products and their recommended usage.

### *6.5.1. Material Models*

Micro-macro CDM material model

- This model was deemed too complicated and potentially inaccurate for the purposes of this study, thus a working version only exists as a Matlab script.
- For simple loading conditions, a strain tensor can be input and the constituent damage can be determined.

Orthotropic CDM Model

- This model is fully documented in SAND2013-7257 [7] and is ready for user applications

Orthotropic Failure Model

- This material model is implemented in Sierra, but only exists on a local machine. Under a separately funded research project, this model will be modified and finalized for production in FY2014.

Transversely Isotropic CDM Model

- This material model is implemented in Sierra, but only exists on a local machine
- If a user is interested in this model, an independent executable can be provided.

### *6.5.2. Meshing*

The following scripts are available:

- Plane Weave Mesh Generator
- Satin Weave Volume Generator
- General Voxel Generator
- Hexagonal Microstructure Mesh Generator
- General Random Microstructure Mesh Generator
- Periodic Random Microstructure Mesh Generator
- Yarn Orient Scripts

### *6.5.3. Simulation and Post-Processing*

Dakota Drive Scripts: for generating and running sample distributions

Input Decks: many different input decks were generated for this study. For much of the analyses presented in this document, the inputs are sorted, but often the mesh and output files were purged.

# 7. CONCLUSIONS AND FUTURE WORK

A brief summary of the conclusions is provided below.

1) Whether implemented for general use or coded to provide a framework for future developments, the material models implemented for this project cover a range of composites damage, plasticity and failure techniques. The generalization of these models is intended to facilitate future use and development. The materials, specifically the orthotropic CDM and elastic fail models, have proven accurate for the intended use outlined in this report.
2) Geometry and mesh generation for plain and harness weave fabric composite RVEs are sufficiently arbitrary for broad use. While, for this project, RVEs are used only with an iso-phase embedded assumption, the generalized form of these scripts should provide usability in an arbitrary layup for large-scale simulations.
3) The micro and mesomechanical approach to elastic property estimation produces excellent results and can be implemented for material selection and design scoping exercises. Furthermore, with proper calibration and model enhancement, these models supplement experimental data and can be used in the design process.
4) Damage and failure assessment using micro and mesomechanical simulations provides insight into processes and adequate properties for preliminary design assessment. However, a fully validated multi-scale modeling approach is an active research field with substantial gaps in understanding. Further research is necessary for implementation as predictive tool.

Numerous future works can be gleaned from this study. In this author's opinion, the most pertinent and attainable are list below:

1) A more generalized RVE approach is needed within Sierra framework. This tool should leave the definition of periodic surfaces completely user defined. Surface combinations, active surfaces and tolerances should be user inputs. Finally, all modeling techniques, such as element death, should be available in the RVE region.
2) A proper understanding of the micromechanisms of failure is crucial for macroscopic characterization. Since micromechanical characterization is available for arbitrary stress/strain states, this technique can be used to determine the complex failure surface. For example: the combined shear and compressive failure is known to have a strong coupling effect. Iterating through various combinations can produce the damage surface.
3) A link from experimental scans to voxel generation and meshing is a valuable endeavor. Potentially, this means that a scan of the meso/micro-structure can indirectly, through modeling, yield elastic parameters. This technique is demonstrated in this project using a 8HS geometry.
4) Sierra's RVE capabilities allows for a user defined coordinate system in the reference mesh. The region internally transforms the strain rate tensor into local coordinates before applying them to the RVE model. Proposed is a laminate

like multi-layer mesh that uses a series of blocks each defined with an orientation and RVE model. The result is laminate like behavior in the reference model, with the individual constitutive response of the layers obtained from the transformed volume average response of the RVEs.

# 8. REFERENCES


[1] E. Barbero, *Finite element analysis of composite materials,* Boca Raton: CRC Press, 2008.

[2] E. Barbero, and L. D. Vivo, "A constitutive model for elastic damage in fiber-reinforced PMC lamina," *Int. J. of Dam. Mech.,* vol. 10, pp. 73-93, 2001.

[3] N. Hansen, and H. Schreyer, "A thermodynamically consistent framework for theories of elastoplasticity coupled with damage," *Int. J. Solids Struct.,* vol. 31, pp. 359-389, 1994.

[4] P. Maimí, P. Camanho, J. Mayugo, and C. Dávila, "A continuum damage model for composite laminates: Part I – Constitutive model," *Mech. of Mat.,* vol. 39, pp. 897-908, 2007.

[5] P. Maimí, P. Camanho, J. Mayugo, and C. Dávila, "A continuum damage model for composite laminates: Part II – Computational implementation and validation," *Mech. of Mat.,* vol. 39, pp. 909-919, 2007.

[6] Y. Thollon, and C. Hochard, "A general damage model for woven fabric composite laminates up to first failure," *Mech. of Mat.,* vol. 41, pp. 820–827, 2009.

[7] S. English, and A. Brown, "A 3D Orthotropic Elastic Continuum Damage Material Model," *SAND2013-7257,* 2013.

[8] E. Barbero, G. Abdelal, and A. Caceres, "A micromechanical approach for damage modeling of polymer matrix composites," *Comp. Struct.,* vol. 67, pp. 427-436, 2004.

[9] P. Maimi, J. Mayugo, and P. Camanho, "A Three-dimensional Damage Model for Transversely Isotropic Composite Laminates," *J. of Comp. Mat.,* vol. 42, pp. 2717- 2745, 2008.

[10] T. Belytschko, W. Liu, and B. Moran, *Nonlinear Finite Elements for Continua and Structures,* West Sussex, England: John Wiley & Sons, 2009.

[11] R. Hill, "A theory of the yielding and plastic flow of anisotropic metals," *Proc. Roy. Soc.,* vol. 193, pp. 281–297, 1948.

[12] Z. P. Bazant, and B. H. Oh, "Crack band theory for fracture of concrete," *Matériaux et Construction,* vol. 16, pp. 155-177, 1983.

[13] S. M. Team, *Lame Material Modelers using Material Failure,* Sandia National Labs., 2011.

[14] G. W. Wellman, "A 3D Orthotropic Elastic Continuum Damage Material Model," *SAND2012-1343,* 2012.

[15] H. T. Hahn, and S. W. Tsai, "On the behavior of composite laminates after initial failures," *J. of Comp. Mat.,* vol. 8, pp. 288 - 305, 1974.

[16] C. Landis, I. Beyerlein, and R. McMeeking, "Micromechanical simulation of the failure of fiber reinforced composites," *J. of the Mech. and Phy. of Solids,* vol. 48, pp. 621-648, 2000.

[17] K. Searles, G. Odegard, and M. Kumosa, "Micro- and mesomechanics of 8-harness satin woven fabric composites: I - evaluation of elastic behavior," *Comp. Part A,* vol. 32, pp. 1627-1655, 2001.

[18] A. Maligno, "Finite Element Investigations on the Microstructure of Composite Materials," *PhD Thesis Univ. of Nottingham,* 2007.

[19] T.-E. Tay, V. Tan, and G. Liu, "A new integrated micro–macro approach to damage and fracture of composites," *Mat. Sci. and Eng.,* vol. 132, pp. 138-142, 2006.

[20] M. Werwer, A. Cornec, and K. Schwalbe, “Local strain fields and global plastic response of continuous fiber reinforced metal-matrix composites under transverse loading,” *Compu. Mat. Sci.,* vol. 12, pp. 124-136, 1998.

[21] E. Totry, C. Gonza´lez, and J. LLorca, “Failure locus of fiber-reinforced composites under transverse compression and out-of-plane shear,” *Compu. Sci. and Tech.,* vol. 68, pp. 829-839, 2008.

[22] M. Romanowicz, “Progressive failure analysis of unidirectional fiber-reinforced polymers with inhomogeneous interphase and randomly distributed fibers under transverse tensile loading,” *Comp. Part A,* vol. 41, pp. 1829-1838, 2010.

[23] S. Swaminathan, S. Ghosh, and N. Pagano, “Statistically Equivalent Representative Volume Elements for Unidirectional Composite Microstructures: Part I – Without Damage,” *J. of Comp. Mat.,* vol. 40, pp. 583-604, 2006.

[24] S. Swaminathan, and S. Ghosh, “Statistically Equivalent Representative Volume Elements for Unidirectional Composite Microstructures: Part II – With Interfacial Debonding,” *J. of Comp. Mat.,* vol. 40, pp. 605-321, 2006.

[25] Z. P. Bazant, “Can multiscale-multiphysics methods predict softening damage and structural failure,” *Int. J. for Multiscale Compu. Eng.,* vol. 8, pp. 61-67, 2010.

[26] C. Heinrich, M. Aldridge, A. S. Wineman, J. Kieffer, A. M. Waas, and K. Shahwan, “The influence of the representative volume element (RVE) size on the homogenized response of cured fiber composites,” *Mod. and Sim. in Mat. Sci. and Eng.,* vol. 20, 2012.

[27] M. Ito, and T. W. Chou, “An analytical and experimental study of strength and failure behavior of plain weave composites,” *J. of Comp. Mat.,* vol. 32, pp. 2-30, 1998.

[28] X. F. Wang, X. W. Wang, G. M. Zhou, and C. W. Zhou, “Multi-scale analyses of 3D woven composite based on periodicity boundary conditions,” *J. of Comp. Mat.,* vol. 41, pp. 1773-1788, 2007.

[29] E. Barbero, T. Damiani, and J. Trovillion, “Micromechanics of fabric reinforced composites with periodic microstructure,” *Int. J. Solids Struct.,* vol. 42, pp. 2489-2504, 2005.

[30] "HexPly® 8552 Epoxy Matrix Product Data," Hexcel Corporation, 2013.

[31] S. Daggumatia, W. V. Paepegema, J. Degriecka, J. Xu, S. V. Lomov, and I. Verpoest, “Local damage in a 5-harness satin weave composite under static tension: Part I – Experimental analysis,” *Comp. Sci. and Tech.,* vol. 70, pp. 1926-1933, 2010.

# APPENDIX A: FOUR VOLUME EDGE GENERATION

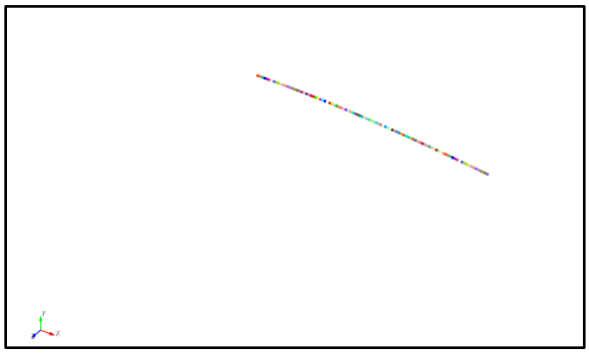

1. Inner fill coss-section/warp path

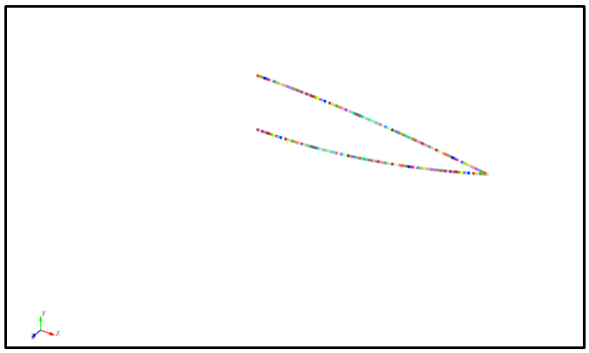

2. Outer fill cross section

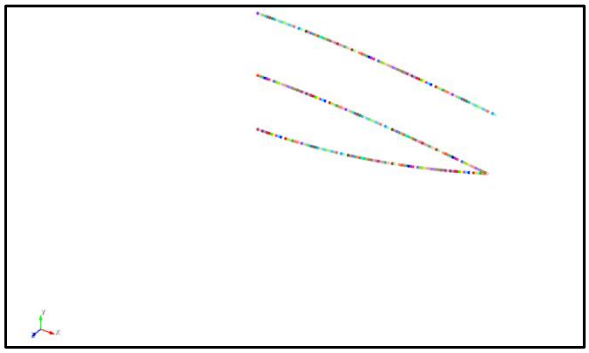

3. Outer warp path

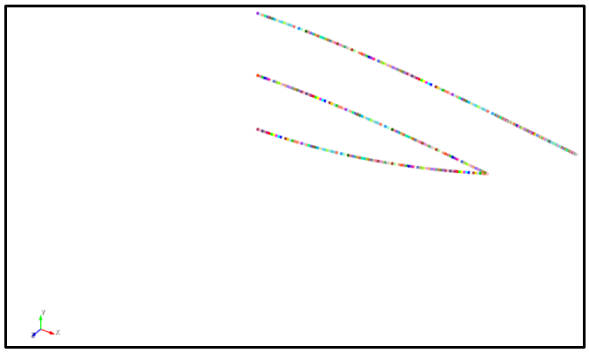

4. Mid outer warp path

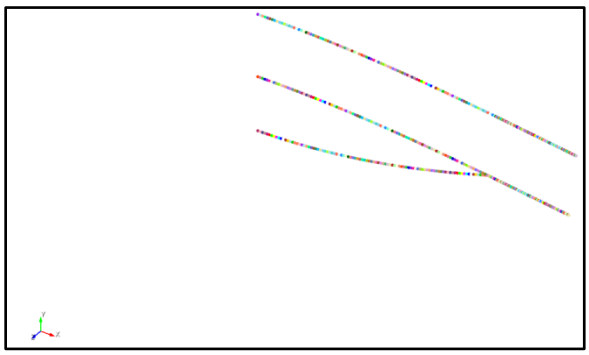

5. Mid inner warp path

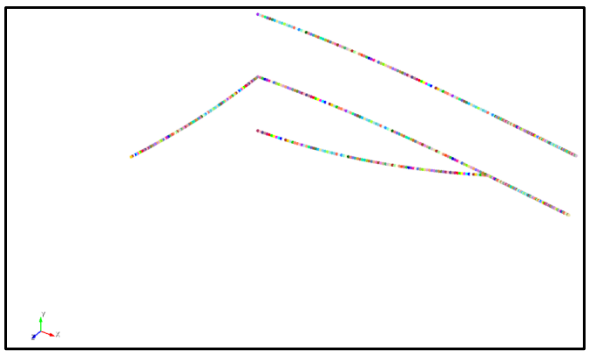

6. Inner warp coss-section/fill path

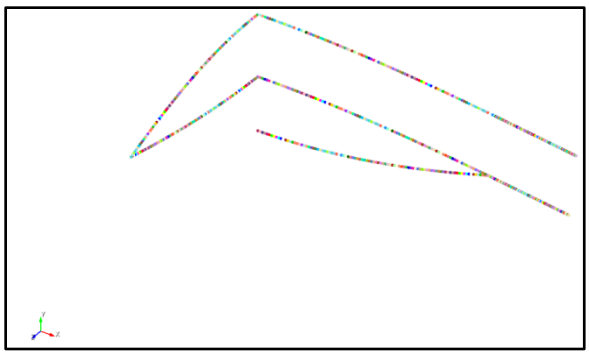

7. Outer warp cross section

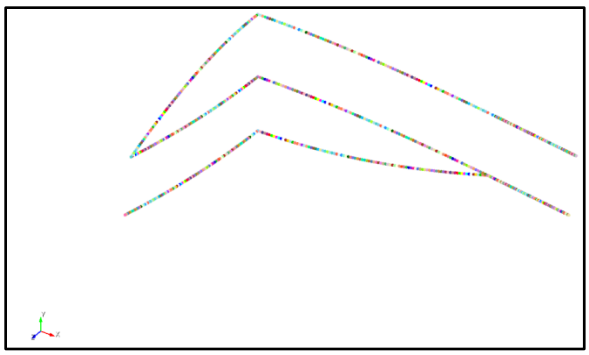

8. Outer fill path

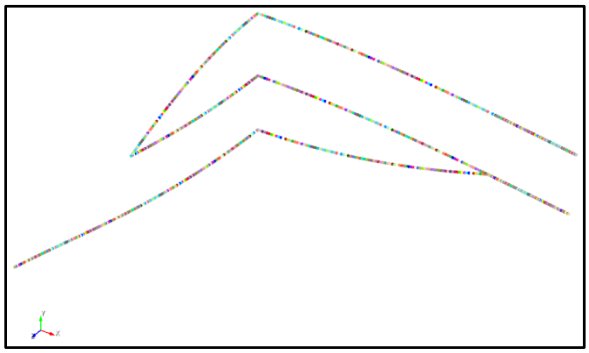

9. Mid outer fill path

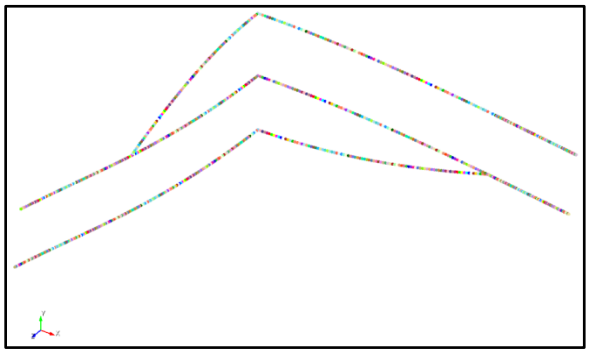

10. Mid inner fill path

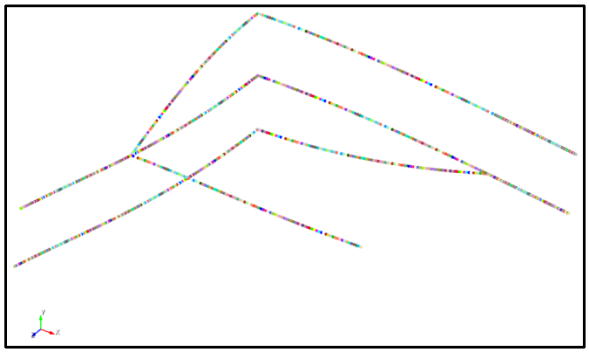

11. Warp edge path/fill cross-section

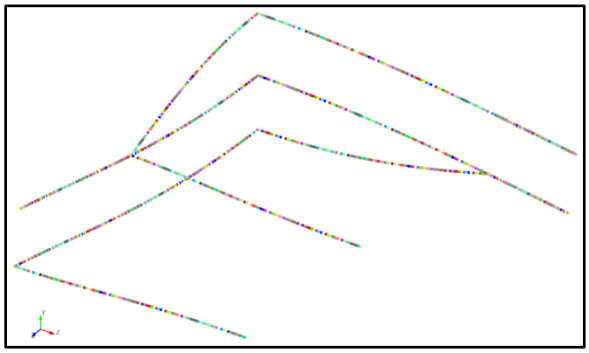

12. Fill cross-section/warp edge path

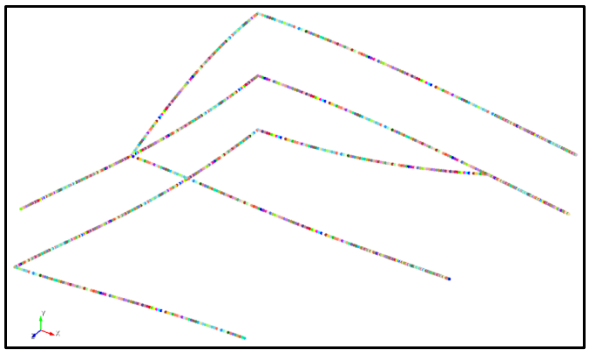

13. Mid warp edge path

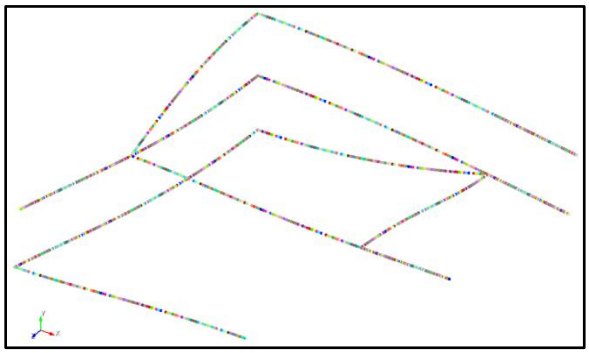

14. Fill edge path/warp cross-section

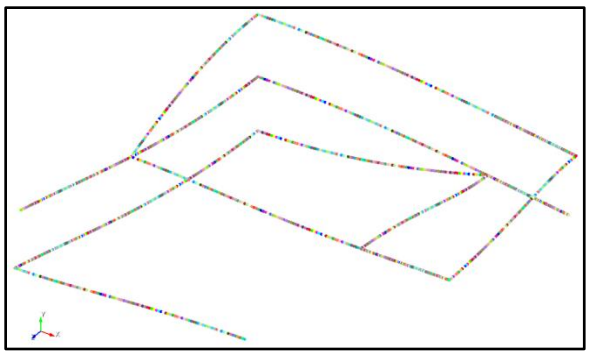

15. Warp cross-section/fill edge path

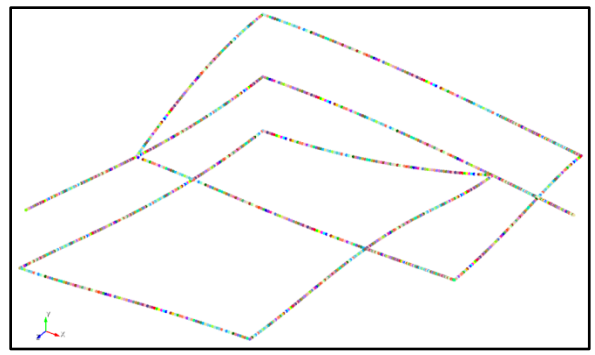

16. Mid fill edge path

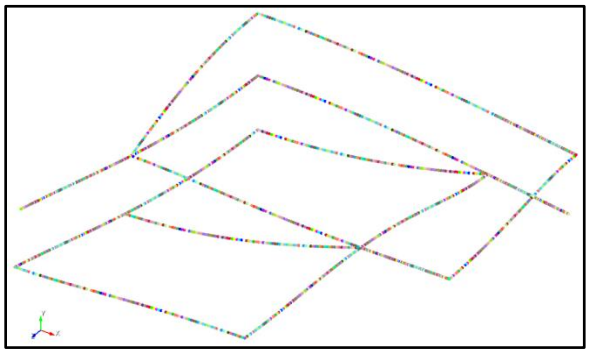

17. Outer fill cross-section

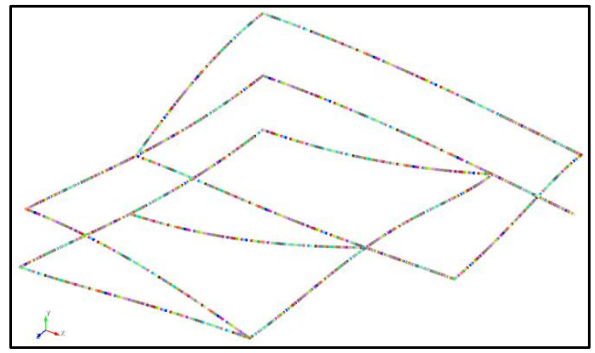

18. Outer fill cross-section

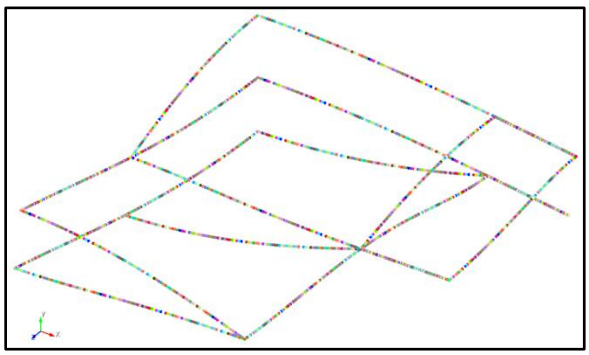

19. Outer warp cross-section

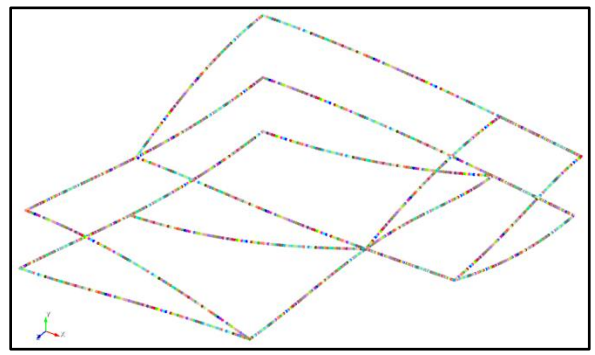

20. Outer warp cross-section

# DISTRIBUTION

| | | | |
|---|---|---|---|
| 1 | MS9042 | M. Chiesa | 8259 (electronic copy) |
| 1 | MS9042 | M. Gonzales | 8250 (electronic copy) |
| 1 | MS9042 | S. Nelson | 8259 (electronic copy) |
| 1 | MS9042 | M. Veilleux | 8259 (electronic copy) |
| 1 | MS9042 | J. Dike | 8259 (electronic copy) |
| 1 | MS9042 | N. Spencer | 8259 (electronic copy) |
| 1 | MS9106 | T. Briggs | 8226 (electronic copy) |
| 1 | MS9042 | J. Foulk | 8256 (electronic copy) |
| 1 | MS0845 | J. Jung | 1542 (electronic copy) |
| 1 | MS0845 | K. Pierson | 1542 (electronic copy) |
| 1 | MS0812 | W. Scherzinger | 1524 (electronic copy) |
| 1 | MS0899 | Technical Library | 9536 (electronic copy) |
| 1 | MS0359 | D. Chavez, LDRD Office | 1911 (electronic copy) |

Sandia National Laboratories